IEEE Access
Multidisciplinary | Rapid Review | Open Access Journal

Received 1 November 2024, accepted 18 November 2024, date of publication 27 November 2024,
date of current version 16 December 2024.

Digital Object Identifier 10.1109/ACCESS.2024.3507673

RESEARCH ARTICLE

Energy Management in Refrigerated Electric Small Transport: A Hierarchical Approach

AGNES POKS, (Member, IEEE), ALEXANDER SCHIRRER, AND MARTIN KOZEK
Institute of Mechanics and Mechatronics, Research Group of Control and Process Automation, TU Wien, 1060 Vienna, Austria

Corresponding author: Agnes Poks (agnes.poks@tuwien.ac.at)

This work was supported in part by the Project "Conserve" Austrian Research Promotion Agency (Forschungsförderungsgesellschaft) (FFG) under Grant 871526, and in part by Technische Universität Wien (TU Wien) Bibliothek Open Access Funding Programme.

ABSTRACT As the delivery industry undergoes a transition with the introduction of small electric transport vehicles, it is crucial to maximize their energy efficiency. Especially for vehicles with cooling chambers, innovative control strategies tailored for the simple onboard hardware are necessary. The presented approach utilizes two-layer optimization, based on an offline optimization layer and a simple real-time controller. Offline optimization prior to the driving mission uses dynamic programming to ensure optimal operation. The approach involves performing backward and forward recursion, computing the cost-to-go matrix at each step by sweeping through the stage variable. The optimal control trajectory is obtained through forward dynamic programming in the second sweep. The optimized offline trajectory is stored onboard the vehicle, defining the control trajectory for a simple real-time control. This approach allows for a holistic optimal energy management using the limited computational resources in existing transport vehicles. Actual vehicle data and realistic driving missions are used for validations. The potential of the proposed control architecture is evaluated in simulations against mixed-integer predictive control and a rule-based proportional-integral controller. Results indicate energy savings ranging from 12.6 to 14.2% and enhancements in temperature regulation from 1.1 to 2.8%.

INDEX TERMS Energy management, hierarchical, dynamic programming, model predictive control, electrical vehicles, mixed-integer, refrigerator system.

I. INTRODUCTION

There are over a million refrigerated road vehicles worldwide, vital for delivering goods to supermarkets and pharmacies daily [1]. The refrigerated transport sector significantly impacts the environment, contributing to 15% of global fossil fuel consumption. The annual increase in the number of refrigerated trucks and the steadily expanding transportation industry intensifies the issue [2], [3]. Last-mile delivery poses particular challenges due to variable conditions [4], [5]. In particular, transitioning to alternative drive-train systems is challenging in the transport sector [6]. Therefore, enhancing the energy efficiency and preventing food waste due to temperature fluctuations while being aware of the technical limitations of the new technologies are key goals of technical advancement [7].

Optimal control strategies for auxiliary consumers, such as cabin heating and battery thermal management, are well-covered in literature [8], [9], [10]. However, there has been limited discussion about small-scale electric trucks that feature an additional cooling chamber. Refrigeration trucks are usually modified after production, and the battery management system does not account for the effect of the cooling chamber. Recent studies presented advanced control strategies that predict disturbances and tackle conflicting goals [7], [11], [12]. However, these studies have only solved individual sub-problems, and no comprehensive approach exists.

The approach presented here addresses all aspects of electric refrigerated transport, including consumption of the drive-train, optimal controller performance, constraint handling and controller tuning, computational load, as well as uncertainties in predictions. This is achieved by a novel hierarchical two-layer comprehensive optimization solution

The associate editor coordinating the review of this manuscript and approving it for publication was Huaqing Li.

for efficient energy and cooling management. Using prior knowledge of the driving mission and driving conditions, an optimal strategy is planned offline. This offline optimization is performed by Dynamic programming (DP), where backward and forward recursion is utilized. Once the optimized offline trajectory is stored onboard the vehicle, a simple real-time control suffices to secure good tracking of the trajectory.

Multiple studies focused on the impact of thermal systems on consumption in combination with the powertrain, especially in electric, hybrid, and fuel cell vehicles [13], [14], [15], [16]. The importance of cabin air conditioning and the influence of auxiliary consumers on energy strategies have been demonstrated there. References [14] and [15] show the high influence on consumption of approx. 20% of the additional cooling. The research conducted in [14] mainly covers the utilization of combustion engines in refrigeration trucks. In turn, [15] has mainly focused on the offline approach and energy consumption for delivery routes.

In comparison to the approach presented here, the studies focus primarily on the thermal management of the integrated battery [17], while others [10], [18] demonstrate thermal management solutions, such as heating and cooling, for passenger cabins of electrified vehicles. Advanced solutions for the vehicle's battery and Heating, ventilation, and air conditioning (HVAC) systems were highlighted in [9], [19], and [20]. However, none of these works presents an advanced solution for an additional refrigeration system. The refrigeration system considered in this work offers a unique approach to the thermal storage (TS) in the shape of a secondary loop (SL), setting it apart from other works. Previous studies have explored the impact and modeling of such a system, including sizing a secondary loop cooling system for refrigerated vehicles [21], [22], [23]. While these studies mainly focused on the SL, the present work considers the complete vehicle system.

Current researches solve similar problems in optimization-based strategies based on optimal control theory to obtain global optimality. While Rule-Based (RB) methods can also be found in literature, their optimality and adaptability for driving conditions are poor, especially for power allocation tasks [24]. The main challenge is finding optimal control strategies for the slow thermal system, which focuses on a long horizon and the complete driving cycle, and on the fast dynamics of the vehicle and battery system, requiring a shorter horizon and a faster computational solution.

Multiple solutions for solving this problem with multi-horizon predictive energy optimization exist. An approach that involves a multi-horizon model predictive control framework for integrated power and thermal management for a fuel cell is given in [8]. Solutions have also been derived for Hybrid Electric Vehicles with different resolutions in the horizon [25], [26] or implementing a shrinking horizon model predictive control (MPC) for long-horizon predictions [9]. Although these works show improvements in battery lifetime and efficiency, all obtain the optimal power strategy by minimizing the MPC cost function under different system constraints. The resulting online computational burden of existing MPC approaches, coupled with their high resource consumption, makes them economically unviable for large-scale or mass-market applications. The trade-off between optimization accuracy and cost remains unresolved in current methodologies. The hierarchical approach proposed in this study aims to address these limitations by offering a more computationally efficient solution. This framework prioritizes computational efficiency and adaptability, overcoming the limitations in real-time execution and economic feasibility.

A different solution is the separation of the dynamics by applying a hierarchical approach in two layers [10], [20]: One optimizing thermal trajectories, the other aiming to enhance energy efficiency without compromising passenger comfort or battery performance. Reference [20] presents a two-layer solution with a nonlinear model predictive controller (NMPC) in each layer, whereas [10] presents a scheduling MPC with long horizon in the upper layer and two tracking MPCs in the lower layer for short horizons. In [27], a linear MPC is used to control the cooling compartment, and a mixed-integer MPC controls three redundant refrigeration systems. These approaches require powerful onboard hardware for online optimization. For long horizons, such as driving missions, the MPC solution achieves only local optimality. Furthermore, refrigeration systems comprise switching elements and, therefore, require mixed-integer (MI) MPC [21].

DP is ideally suited to compute globally optimal solutions for EMS [28], [29], [30]. DP has the advantage of considering nonlinear, non-convex, mixed-integer model characteristics. Powerful offline consumption minimization strategies have been found in the presence of constraints using DP [28], [31], [32]. Optimal offline solutions for a hybrid electric fuel cell using DP combined with online RB control have been presented in [18] and [33]. In [33] a multi-dimensional database that follows the optimal solution by interpolation is given. Real-time implementations of DP have undergone persistent improvement in recent years, especially optimized grid size and state [34], and modeling [35] promises faster computation. Nevertheless, especially for multi-dimensional systems, the computational complexity and demand for prior knowledge of driving conditions make DP rather unsuitable for real-time optimization.

Although MPC provides real-time optimization capabilities ([8], [9]), it comes with significant computational demands. The lack of powerful hardware on current transport vehicles is a challenge that needs to be addressed. Hierarchical control structures, as shown in previous studies, highlight the advantages of separating long-horizon and short-horizon tasks, particularly in thermal management [10], [20]. DP has proven effective in handling nonlinear, non-convex problems in energy management for hybrid and electric vehicles [30], [31], but it has not been efficiently applied to vehicles

with refrigeration units containing thermal storage within a comprehensive system.

The main contributions of this paper are:

1) Dynamic programming is employed to solve the original nonlinear, non-convex, mixed-integer problem offline. This optimization results in a control trajectory for the simple onboard real-time controller with a discretization optimal for systems with strongly differing time-constants.

2) The cost-to-go matrix in the proposed algorithm is computed for each step by backwards DP. The optimal control trajectory is then obtained in a second step by forward DP. If a new optimized trajectory needs to be computed due to disturbances, only the numerically efficient forward recursion must be repeated.

3) Spatial sampling over the driving cycle is used, combined with a time-based model for door openings to accurately account for delivery stops. This enables accurate modeling of power losses during unloading of the vehicle with minimum computational complexity.

Overall, a globally optimal trajectory is followed by a simple real-time control onboard the vehicle, thus ensuring high performance, minimal power consumption, and economically attractive implementation. Comparisons to model predictive control and traditional rule-based control in simulations clearly demonstrate the advantageous charactersitics of the proposed method.

The remainder of the paper is organized as follows: The control strategy is provided in Section II, and system modeling is given in Section III. In Section IV, the offline optimization is presented, and the real-time approach is contained in Section V. In Section VI the alternative controllers for comparison are shortly presented. Simulation results are presented in Section VII to show the performance of the approach. The work ends with a discussion in Section VIII and a conclusion in Section IX.

II. CONTROL STRATEGY

The designed control strategy is a multi-hierarchical optimization-based method (MH-Opt) to address the challenges of real-time optimization, computational load, and global optimality. The illustrated architecture shown in Fig. 1 represents an integrated control system architecture that provides route optimization, a cloud-based offline strategy formulation, and a real-time online control strategy for electric refrigeration vehicles. The specific disturbance of door openings to the cooling chamber is explicitly considered in the offline strategy.

Today's geoinformation systems, together with real-time information on traffic congestion, speed limits, and weather conditions, enable effective route optimization [36], [37].

As shown in Fig. 1, it is assumed that the route of the delivery mission is planned prior to departure. The associated elevation profile can be derived from topographic data. An offline velocity prediction is computed based on a comprehensive vehicle model together with speed limits and traffic information.

An offline optimization utilizes this speed prediction as an input to minimize energy consumption while keeping the temperature inside the cooling chamber within predefined limits. The cost-to-go matrix graphically represents a strategic control framework that enables the determination of an optimal control policy by navigating through different state transitions. Furthermore, the implemented control algorithm includes a prediction for optimal door-opening event handling. The optimal solution is then stored as reference trajectory locally on the vehicle's control unit, see Fig. 1. Note that after the offline strategy delivers an optimized reference and the parameters to the vehicle, no further information flow to the online strategy exists.

During the delivery mission, a computationally simple real-time control acts as a regulator to track the optimal trajectory specified by the offline computation. The parameters of this real-time controller can be optimized by an auto-tuning algorithm, thus incorporating variable load and route characteristics and their respective effect on thermal dynamics. Note that a new offline optimization is only initiated in the event of significant deviations from the optimized trajectory (e.g. sudden congestion due to an accident).

The proposed control strategy facilitates a responsive vehicular system that adapts to real-time events while optimizing energy efficiency, temperature control, and operational parameters. Moreover, only minimal data storage, computational power, and communication bandwidth are required onboard the delivery vehicle.

III. SYSTEM MODELING

This section provides a description of the system in mathematical terms and serves as the basis for the optimization model discussed in subsequent sections.

1) SYSTEM ARCHITECTURE AND BOUNDARIES

The principal objective of the control system is to globally meet the load demand, such as maintaining the cooling chamber's temperature at a set value or ensuring that the outlet temperature of the evaporator's secondary loop follows a specified reference trajectory. In the context of an electric vehicle's powertrain, this goal corresponds to effective thermal management that aims for the sustainable operation of the battery. The complete system is presented in Fig. 2.

The electric powertrain, powered by a battery pack and overseen by a Battery Management System (BMS), incorporates an electric motor with AC / DC converters that allow the system to charge during recuperation [38], [39]. It is also equipped with auxiliary systems and storage (AUX), a secondary loop refrigeration unit that works as thermal storage (TS) and an Internal Cooling Chamber (ICC), critical for regulating temperatures of the delivered goods, denoted by the power flows (P) from and the thermal transfers (Q) within the system.

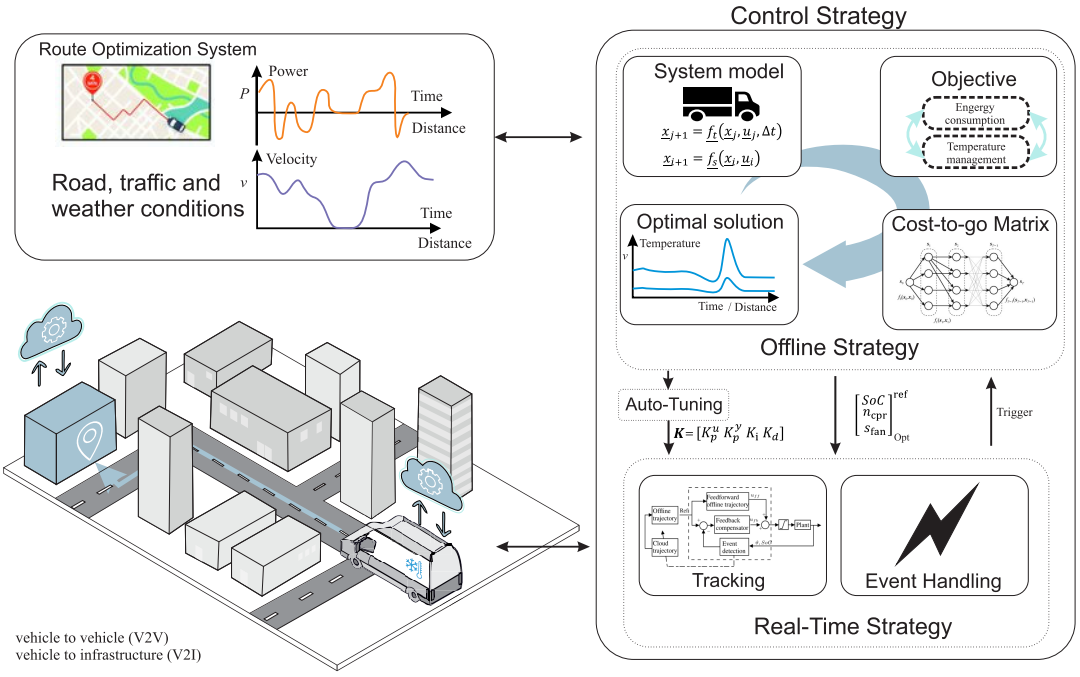

FIGURE 1. Overview of the proposed control strategy for offline and real-time controller architecture.References and parameter vector K are sent to the real-time controller at the initialization of the control algorithm. A simple real-time controller performs tracking of the optimized reference. When events occur (characterized by strong deviations from the optimized values) the offline optimization is performed again, and a new initialization is done.

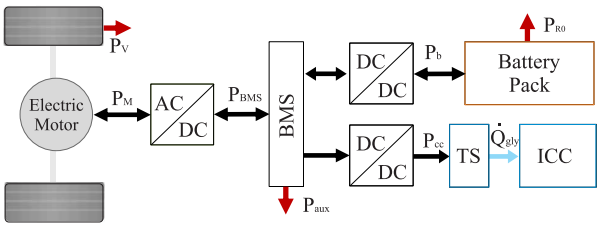

FIGURE 2. Architecture of the electric powertrain of the vehicle. Legend: battery management system (BMS), auxiliary systems (AUX), secondary loop thermal storage (TS), and internal cooling chamber (ICC).

2) SECONDARY LOOP REFRIGERATION SYSTEM

In this section, the mathematical model of the refrigeration system (RS) with a secondary loop is described. The model is based on [21] and [22] with some adaptations for offline optimization. The system is described by the following non-stationary balance equations in continuous time t:

$$\begin{aligned}\frac{d}{dt}\vartheta_{\mathrm{cc}}(t) = {} & \xi_1\left[\dot{Q}_{\mathrm{z}}(t) - \dot{Q}_{\mathrm{ac}}^{\mathrm{aug}}(t)\right] + \dots \\ & \xi_2\left[\vartheta_{\mathrm{w}}(t) - \vartheta_{\mathrm{cc}}(t)\right] + \dots \\ & \xi_3\left[\vartheta_{\mathrm{amb}}(t) - \vartheta_{\mathrm{cc}}(t)\right] + \dot{Q}_{\mathrm{door}}(t) \end{aligned} \tag{1}$$

$$\frac{d}{dt}\vartheta_{\mathrm{gly}}^{\mathrm{out}}(t) = \chi_1\left[\vartheta_{\mathrm{gly}}^{\mathrm{in}}(t) - \vartheta_{\mathrm{gly}}^{\mathrm{out}}(t)\right] + \chi_2\,\dot{Q}_{\mathrm{ac}}(t) \tag{2}$$

$$\frac{d}{dt}\vartheta_{\mathrm{w}}(t) = -\zeta_1\left[\vartheta_{\mathrm{w}}(t) - \vartheta_{\mathrm{cc}}(t)\right] \tag{3}$$

with temperatures inside the chamber $\vartheta_{\mathrm{cc}} \in \mathbb{R}$, water–glycol mixture $\vartheta_{\mathrm{gly}} \in \mathbb{R}$, of the wall $\vartheta_{\mathrm{w}} \in \mathbb{R}$ and ambient air $\vartheta_{\mathrm{amb}} \in \mathbb{R}$. Parameters $\xi_i \in \mathbb{R}_{\geq 0}$, $i \in \{1, 2, 3, 4\}$ include the properties associated with heat transfer on contact surfaces. The parameters $\chi_i \in \mathbb{R}$, $i \in \{1, 2, 3\}$ implicitly include the heat capacity of the water-glycol mixture. The properties of the wall (thermal capacity, thermal conductivity, thickness) are defined through $\zeta_1 \in \mathbb{R}_{\geq 0}$. In addition, heat flows are defined for loads $\dot{Q}_{\mathrm{z}} \in \mathbb{R}$, the heat exchanger $\dot{Q}_{\mathrm{he}} \in \mathbb{R}$, the air chiller $\dot{Q}_{\mathrm{ac}} \in \mathbb{R}$, and for disturbances $\dot{Q}_{\mathrm{door}} = \xi_4\left[\vartheta_{\mathrm{amb}}(t) - \vartheta_{\mathrm{cc}}(t)\right] s_{\mathrm{door}}(t)$.

As the fluid enters the heat exchanger with temperature $\vartheta_{\mathrm{gly}}^{\mathrm{out}}$, undergoes cooling, and leaves the heat exchanger with temperature $\vartheta_{\mathrm{gly}}^{\mathrm{in}}$, the relation is given as

$$\vartheta_{\mathrm{gly}}^{\mathrm{in}}(t) = \vartheta_{\mathrm{gly}}^{\mathrm{out}}(t) - \chi_1\,\dot{Q}_{\mathrm{he}}^{\mathrm{arb}}(t), \tag{4}$$

$$\begin{aligned}\dot{Q}_{\mathrm{he}}^{\mathrm{arb}}(t) = {} & \left[\alpha_1\, n_{\mathrm{cpr}}(t) - \alpha_2\,\vartheta_{\mathrm{amb}}(t) + \dots\right. \\ & \left.\alpha_3\,\vartheta_{\mathrm{gly}}^{\mathrm{out}}(t) - \alpha_4\right] \end{aligned} \tag{5}$$

parameters referring to the cooling loop are denoted by $\alpha_i \in \mathbb{R}_{\geq 0}$, $i \in \{1, 2, 3, 4\}$ and the compressor speed input by n_{cpr}.

The air chiller fan's status determines the heat transfer $\dot{Q}_{\mathrm{ac}}$ in the heat exchanger between water-glycol mixture and air:

$$\begin{aligned}\dot{Q}_{\mathrm{ac}}(t) = {} & \beta_1\left[\vartheta_{\mathrm{cc}}(t) - \vartheta_{\mathrm{gly}}^{\mathrm{in}}(t)\right] s_{\mathrm{fan}}(t) + \dots \\ & \beta_2\left[\vartheta_{\mathrm{cc}}(t) - \vartheta_{\mathrm{gly}}^{\mathrm{in}}(t)\right]\left[1 - s_{\mathrm{fan}}(t)\right], \end{aligned} \tag{6}$$

where $\beta_1 \in \mathbb{R}_{\geq 0}$ and $\beta_2 \in \mathbb{R}_{\geq 0}$ represent the heat transfer in case of forced and free convection, respectively. The binary system inputs are the fan switch and door opening, where $s_i \in \{0, 1\}$, $i \in \{\mathrm{fan}, \mathrm{door}\}$.

The effect of the cooling unit on the inside air is given by the augmented air chiller heat flow $\dot{Q}_{\text{ac}}^{\text{aug}} \in \mathbb{R}$:

$$\begin{aligned}\dot{Q}_{\text{ac}}^{\text{aug}}(t) = \; & \dot{Q}_{\text{ac}}(t) - P_{\text{fan}}(t) \; - \ldots \\ & [-\gamma_1 \, \vartheta_{\text{cc}}(t) + \gamma_2] \; s_{\text{fan}}(t) \; - \ldots \\ & [\;\; \gamma_3 \, \vartheta_{\text{cc}}(t) + \gamma_4] \; [1 - s_{\text{fan}}(t)]\end{aligned} \tag{7}$$

with $\gamma_i \in \mathbb{R}_{\geq 0}$, $i \in \{1, 2, 3, 4\}$ air chiller parameters and the electrical power input to the air chiller fan,

$$P_{\text{fan}}(t) = \kappa_1 \, s_{\text{fan}}(t) \tag{8}$$

where the parameters of the power consumption model are labeled by $\kappa_i \in \mathbb{R}_{\geq 0}$, $i \in \{1, 2, \ldots, 6\}$.

The compressor power is approximated by an affine approach as

$$\begin{aligned}P_{\text{cpr}}(t) = \big[& \kappa_2 \, n_{\text{cpr}}(t) + \kappa_3 \, \vartheta_{\text{amb}}(t) + \ldots \\ & \kappa_4 \, \vartheta_{\text{cc}}(t) - \kappa_5 \big] .\end{aligned} \tag{9}$$

The total electrical power demand thus follows to

$$P_{\text{cc}}(t) = P_{\text{fan}}(t) + P_{\text{cpr}}(t) + \kappa_6, \tag{10}$$

with $\kappa_6 \in \mathbb{R}_{\geq 0}$ representing an arbitrary auxiliary power parameter.

3) LONGITUDINAL VEHICLE MODEL

The longitudinal vehicle model considers the traction, aerodynamic drag, rolling resistance, and gravitational force and is expressed by Newton's second law for motion

$$m_t \frac{dv(t)}{dt} = F_{\text{eng}} - F_{\text{drag}}, \tag{11}$$

where m_t is the mass of the vehicle, $\frac{dv}{dt}$ is the acceleration, v is the speed, and F_{eng} is the total traction force. Driving resistance F_{drag} is estimated using data obtained from coast-down tests [40]. Thus, fitting the drag force to a polynomial function of speed results in, see [41]:

$$\begin{aligned}F_{\text{drag}}(v) &= C_0 + C_1 v + C_2 v^2 \\ C_0 &= [m_t g \, (\mu_0 \cos\theta + \sin\theta) + \frac{1}{2} \rho c_d A_v w^2] / m_{\text{ap}} \\ C_1 &= \left(m_t g \mu_1 \cos\theta + \frac{1}{2} \rho c_d A_v w \right) / m_{\text{ap}} \\ C_2 &= \left(\frac{1}{2} \rho c_d A_v \right) / m_{\text{ap}}\end{aligned} \tag{12}$$

where g is the acceleration due to gravity, and θ is the road slope angle. In addition, ρ is the density of air, c_d is the drag coefficient, A_v is the frontal area of the vehicle, μ_0 is the coefficient of rolling resistance, μ_1 inflation-pressure (truck tires $\mu_1 = 0.2$ s/m). m_{ap} is the mass influenced by rotating parts that can be approximated by $m_{\text{ap}} = m_t \cdot 1.03$, and w is the wind velocity in the longitudinal direction [42].

The traction power $P_{\text{V}}(t)$ of the electric motor can be expressed by the net engine force, the braking force, and the vehicle speed:

$$P_{\text{V}}(t) = (F_{\text{brake}} + F_{\text{eng}}) v(t) \tag{13}$$

4) BATTERY MODEL

Power losses of the battery P_{R0} are caused by the internal resistance R_0 [43], [44]:

$$P_{R0} = R_0 I_b^2 = R_0 \frac{V_{OC} - \sqrt{V_{OC}^2 - 4 P_b R_0}}{2 R_0} \tag{14}$$

In Eq. (14) the open-circuit voltage V_{OC} is approximated by a polynomial function of the state-of-charge SoC:

$$V_{OC} = a_1 SoC(t)^3 + a_2 SoC(t)^2 + a_3 SoC(t) + a_4, \tag{15}$$

where $a_i \in \mathbb{R}_{\geq 0}$, $i \in \{1, 2, 3, 4\}$. The $SoC(t)$ is the ratio between the actual charge, $Q = -\int I_b dt$, and the nominal charge (or capacity), Q_{nom}.

The total electric power $P_b(t)$ is defined as the sum of motor power, refrigeration power, auxiliary system power consumption, and included ohmic losses. To accommodate for the power losses occurring in the inverter, electric motor, power converters, and drive-train components, an efficiency factor $\eta^{-\text{sgn}(P_{\text{V}})}$ is introduced, which is distinct for the charging and discharging processes:

$$P_b(t) = \eta^{-\text{sgn}(P_{\text{V}})} P_V(t) + P_{\text{aux}}(t) + P_{\text{cc}}(t) \tag{16}$$

The rate of change of SoC is proportional to the battery current, and the non-stationary balance equation for the battery is given by:

$$\frac{dSoC(t)}{dt} = \frac{-I_b \eta^{-\text{sgn}(P_{\text{V}})}}{Q_{nom}} = \eta^{-\text{sgn}(P_{\text{V}})} \frac{V_{OC} \sqrt{V_{OC}^2 - 4 P_b R_0}}{2 Q_{nom} R_0} \tag{17}$$

5) COMPLETE SYSTEM MODEL

The complete system description results by combining the differential equations (1)-(3) and (17). The state variable is defined as $\boldsymbol{x} = [\vartheta_{\text{cc}}(t) \; \vartheta_{\text{gly}}(t) \; \vartheta_{\text{w}}(t) \; SoC(t)]^T$ and the control variable as $\boldsymbol{u} = [n_{\text{cpr}}(t) \;\; s_{\text{fan}}(t)]^T$, and the disturbance as $\boldsymbol{z} = [P_b(t) \; s_{\text{door}}(t)]^T$. The nonlinear system can be expressed as a state space equation:

$$\begin{aligned}\dot{\boldsymbol{x}}(t) &= f_{\text{dyn}}(\boldsymbol{x}(t), \boldsymbol{u}(t), \boldsymbol{z}(t)) \\ \boldsymbol{y}(t) &= \boldsymbol{C}\boldsymbol{x}(t)\end{aligned} \tag{18}$$

IV. OFFLINE TRAJECTORY OPTIMIZATION

In this Section, the computation of the offline trajectory is explained. After an overview on DP the specific implementation is described, and event-handling for door-openings and delays caused by traffic is explicated.

A. OVERVIEW ON DYNAMIC PROGRAMMING

DP is a well-known optimization method based on Bellman's principle of optimality [45]. It outperforms many other optimization methods due to its ability to handle multi-objective/multi-variable problems and to acquire the global optimal solution based on receding cost minimization, where complex problems are broken down into smaller sub-problems [46]. These smaller sub-problems can be

independently solved, leading to efficient algorithms for many problems. However, for real-time applications with long horizons DP can be computationally too expensive. Furthermore, incorporating multi-state multi-control variables can pose challenges, as mentioned in [30] and [47]. Due to computational advancements such as the vectorized method [48], along with improvements in optimal grid design [49] and suitable model description [35], the DP algorithm offers a viable approach for offline trajectory optimization.

B. IMPLEMENTATION OF THE DP ALGORITHM

1) DISCRETE DYNAMIC SYSTEM

The discrete dynamic system is described by (18). Each continuous state is discretized into finite points, where the size of the state grid set $\mathcal{X}$ and action grid set $\mathcal{U}$ depends on the respective boundaries (hard constraints) of the system and the increment Δ of the discretization.

The discretization method used is a fourth-order Runge-Kutta (RK4) algorithm. A discretization of the states describing the temperatures of Δx_i=0.4 °C, with i $\in \{1, 2, 3\}$ was selected, corresponding to the sensor accuracy, and for the state of charge of Δx_4=0.01. For the control input variables, a discretization of $\Delta u_1 = 200$ rpm was chosen for the compressor, aligned with the specifications of the compressor used in the subsequent comparisons in simulation. As the fan is a binary state, Δu_2=1 is selected. Using the linear interpolation method in the DP forwards solution, feasible solutions can be achieved between discrete grid points. The driving cycle is discretized for the entire distance ranging from 0 to the end value defined as $\mathcal{S}$ with a resolution of Δs=20m to accurately cover urban areas. Additionally, extra discretization points are introduced at door openings, right before and immediately after the stop, to improve resolution during critical events. For a more detailed examination of the optimal discretization, which impacts both computational cost and accuracy, we refer to the relevant literature [49].

2) COST FUNCTIONS

There are two different costs introduced to formulate the total cost J_s for a specific distance step s during travel: The running cost $g(\boldsymbol{x}, u)$, which occurs at each step from distance 0 to $\mathcal{S} - 1$, and the terminal cost $G(\boldsymbol{x})$ that occurs only at the end of the journey. In the following, all variables used in cost functions are normalized using the Min-Max scaling. Furthermore, the running cost consists of several parts which should cover different control aspects.

The running cost for the reference temperature and the power losses is defined as follows:

$$g(\boldsymbol{x}, \boldsymbol{u})_1 = \|x_1 - x_{1,\text{ref}}\|^2_{Q_1} + \|x_4\|^2_{Q_2} + Q_3 P_{R0}(P_b, u) \tag{19}$$

In addition, running costs for a temperature window are also defined as soft constraints to the running cost as follows.

$$g(\boldsymbol{x}, \boldsymbol{u})_2 = \begin{cases} Q_4, & \text{if } |x_1| > x_{1,\text{ref}} \times (1 + \Delta x_1) \\ 0, & \text{otherwise} \end{cases} \tag{20}$$

Additional costs are incurred as the battery state of charge SoC approaches the minimal value. Further costs are also incurred for the water-glycol thermal storage to prevent damage to the water pump:

$$g(\boldsymbol{x}, \boldsymbol{u})_3 = \begin{cases} Q_5, & \text{if } x_{2,4} < x_{2,4^{\min}} + \Delta x_{2,4} \\ 0, & \text{otherwise} \end{cases} \tag{21}$$

For all states, higher costs will also be accounted for when they reach the defined boundaries:

$$g(\boldsymbol{x}, \boldsymbol{u})_4 = \begin{cases} Q_6, & \text{if } \sum_{i=1}^{4} \left(x_i > x_{i_{\max}} \vee x_i < x_{i_{\min}}\right) \\ 0, & \text{otherwise} \end{cases} \tag{22}$$

Since the vehicle and the refrigeration system use the same battery, there exists also a maximum power constraint:

$$g(\boldsymbol{x}, \boldsymbol{u})_5 = \begin{cases} Q_7, & \text{if } P_\text{b} \geq P_{\text{b}^{\max}} \\ 0, & \text{otherwise} \end{cases} \tag{23}$$

The terminal cost function is defined as:

$$G(\boldsymbol{x}_S) = \|x_1 - x_{1,S}\|^2_{Q_8} + \|x_4 - x_{4,S}\|^2_{Q_9} \tag{24}$$

Each weighting, denoted as $Q_i \in \mathbb{R}_{\geq 0}$ where $i \in \{1, 2, \ldots, 9\}$, is chosen based on the control objective: either energy consumption can be minimized or control quality can be maximized. A good balance between these objectives is usually desirable.

3) DEFINITION OF THE DP OPTIMIZATION

The DP algorithm can be formulated in a compact way. For every combination of initial state vectors $\boldsymbol{x_0}$, the total cost $J_s(\boldsymbol{x}_0)$ is equal to $J_s(\boldsymbol{x}_s)$, which is given by the last step of the algorithm and proceeds backward in time from period $S-1$ to period 0.

$$J_s(\boldsymbol{x}_s, \boldsymbol{u}_s) = \begin{cases} \sum_{i=1}^{5} g(\boldsymbol{x}_s, u_s)_i + J_{s+1}(f(\boldsymbol{x}_s, \boldsymbol{u}_s)) & s \neq S \\ G(\boldsymbol{x}_S) & s = S \end{cases} \tag{25}$$

Optimal offline optimization aims to minimize battery power losses for the planned trip and maintain the temperature window while considering system dynamics, as well as physical hard and operational soft constraints. The optimal

optimization problem can be stated as follows:

$$\begin{aligned} \min_{u_s \in U_s(x_s)} \quad & J_s(\boldsymbol{x}_s, \boldsymbol{u}_s) \\ s.t. \quad & x_{s+1} = f_{\text{dyn}}(\boldsymbol{x}_s, \boldsymbol{u}_s, \boldsymbol{z}_s) \\ & \boldsymbol{x}_{s+1} \in \chi_{s+1}, \quad s = 1, \ldots, S \\ & \boldsymbol{u}_s \in \mathcal{U}, \quad s = 1, \ldots, S \\ & \forall \boldsymbol{x}_s \in \mathcal{X}, \quad s = 1, \ldots, S \\ & \forall s \in \mathcal{S} \end{aligned} \tag{26}$$

The sets $\mathcal{U}$ and $\mathcal{X}$ are obtained by quantizing the states and inputs of the system, respectively. These sets consist of feasible values that adhere to the system's specified constraints, including hard and soft constraints for temperature windows and maximum battery power, state of charge, and terminal temperature.

The result of the optimization is an optimal action matrix $\mathcal{U}$, and an optimal state matrix of $\mathcal{X}_{opt}$ also a multidimensional cost the cost-to-go matrix, for each quantization step $s \in \mathcal{S}$.

4) DP ALGORITHM

Fig. 3 illustrates the algorithm to determine the best control trajectories for the cooling chamber of a refrigerated truck. It incorporates both backward and forward calculations.

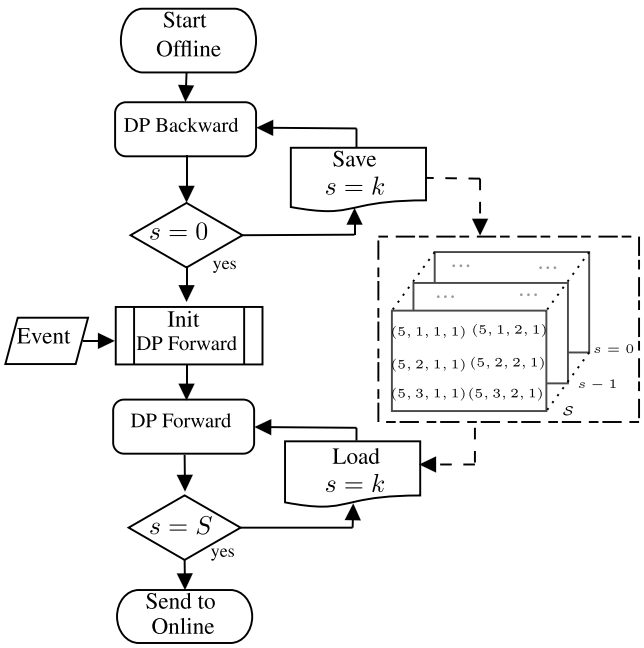

FIGURE 3. DP algorithm explanation for backward and forward calculations on a refrigerator truck.

During the DP backward phase, computations are executed in a reverse sequence. The cost-to-go for each state in the state space is calculated using the cost function Eq. (25) and the available action space to create a cost-to-go matrix for each point in the grid in the state space $\mathcal{S}$. The DP backward loop continues until the starting point of the driving cycle $s = 0$ is reached. Additionally, transition costs between all states are calculated and stored in lookup tables for the forward algorithm and the event handling during real-time operation.

In the DP forward phase, the algorithm begins at the current position in the driving cycle, $x_0 = x_s$, and continues until the end S. At each step s, the lookup tables are loaded with the feasible state set $\mathcal{X}$, the action set $\mathcal{U}$, and the cost-to-go matrix. The DP forward algorithm then identifies the lowest cost and the optimal action.

Deviations from the original optimized trajectory can be detected by defining simple thresholds. This can be caused by closed streets, traffic jams, etc. In that case, an event triggers an updated DP forward computation. It utilizes the stored-state matrices from the backward phase and progresses with forward calculations, initializing the system with the current measured state.

The new optimal control trajectory is sent to the delivery vehicle, allowing optimal operation under changed conditions. In order to ease understanding of the computations and the information flow of the offline algorithm, the pseudo-code of this algorithm is presented in Algorithm 1.

Algorithm 1 Pseudo-Code DP Algorithm

Input: Δ: grid sizes; S: total steps; $\mathcal{M}$: driving missions
initialize state and action grids $\boldsymbol{x}_0$, $\boldsymbol{u}_0$,$\boldsymbol{J}$
define costs $G(\boldsymbol{x}_S)$, $\boldsymbol{g}_(\boldsymbol{x}, \boldsymbol{u})$
for $s = S - 1$ to 0 **do** ▷ Backward phase
  for each state $\boldsymbol{x}_s$ in state space $\mathcal{S}$ **do**
    for each control input $\boldsymbol{u}_s$ in action set $\mathcal{U}$ **do**
      $\boldsymbol{x}_s \leftarrow f_{\text{dyn}}(\boldsymbol{x}_s, \boldsymbol{u}_s, \boldsymbol{z}_s)$ update state transition costs
      $J_s(\boldsymbol{x}_s, \boldsymbol{u}_s) \leftarrow$ compute cost matrix and store
      $\mathcal{U}, \mathcal{X} \leftarrow \boldsymbol{u}_s$ store state, input in sets
    end for
  end for
end for
ifevent detect $\wedge\varnothing \leftarrow$ optimal reference **then**
  set initial state $\boldsymbol{x}_s = \boldsymbol{x}_0$ ▷ Forward phase
  for $s = 0$ to S **do**
    $\boldsymbol{x}_s, \boldsymbol{u}_s, \boldsymbol{J}_s \leftarrow \mathcal{X}, \mathcal{U}, \boldsymbol{J}$ load sets and cost matrix
    $u_s \leftarrow \text{argmin}\boldsymbol{J}_s(\boldsymbol{x}_s)$ optimal control for minimum cost
    $\boldsymbol{x}_{s+1} = f_{\text{dyn}}(\boldsymbol{x}_s, u_s, \boldsymbol{z}_s) \leftarrow$ update state
  end for
end if
Return:optimal reference

C. EVENT HANDLING

In Fig. 4a a typical vehicle loading/unloading scenario is shown. In the top sub-plot, the vehicle is at a stop. The bottom sub-plot represents the state-space with velocity as the vertical axis and distance on the horizontal axis. The state space is discretized into $\mathcal{X}_{\text{bins}}$, and the transition

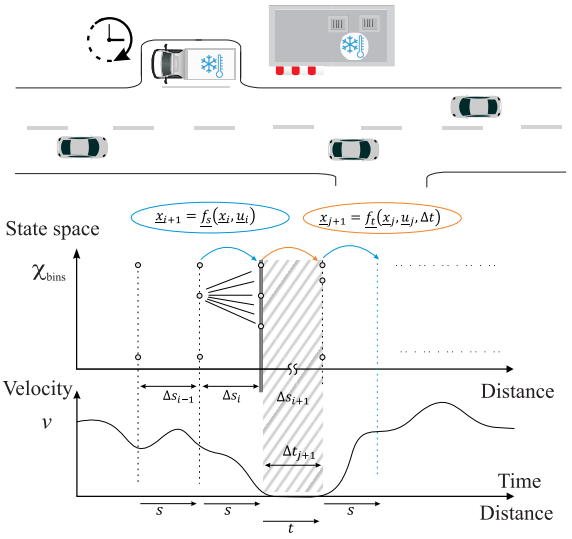

(a) Stop scenario: during a stop scenario the space-based control is shifted to a time-based formulation, taking into account the door opening time by setting the initial state based on a lookup-table.

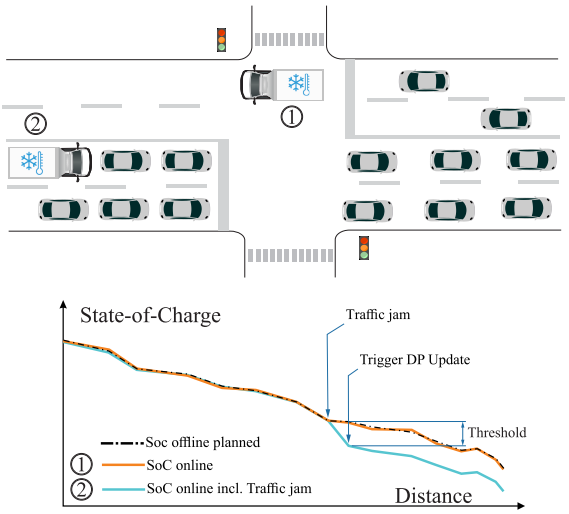

(b) Traffic scenario: ① shows the traffic free case where the vehicle drives accordingly to the offline trajectory. ② shows the case where the vehicle stuck in a traffic jam which causes a deviation from the offline planned trajectory → threshold triggers recalculation of forward dynamic programming.

FIGURE 4. Exception Handling for different driving scenarios.

functions $f(x_k, u_k)$ and $f(x_k, u_k, \Delta t)$ are depicted. These functions describe the system's progression over time with and without the inclusion of time increments Δt, respectively. The shaded regions, Δs_i and Δs_{i+1}, denote the spatial change over discrete time intervals, illustrating the system's transition across states. Notably, the diagram signifies a shift from space-based to time-based control during a stop, incorporating the door opening time by initializing the state using a lookup table.

In Section IV-C two cases for event triggering are shown, illustrating the adaptive management of a vehicle's *SoC* in response to varying traffic conditions. The upper portion of the diagram depicts a specific event. The right sub-plots describe two cases: the first is traffic-free, where the vehicle follows a pre-planned, optimal path as indicated by label 1. The second case, labeled 2, shows the vehicle caught in an unexpected traffic jam, leading to a departure from the pre-planned trajectory.

In the lower right sub-plot, the vehicle's *SoC* is plotted against the distance traveled. Two *SoC* trajectories are depicted: the dashed line represents the planned *SoC* levels under traffic-free conditions, while the solid line represents the actual *SoC* trajectory, which includes the impact of a traffic jam. When a threshold is crossed, it triggers an update in the DP algorithm (forward computation only). The diagram visualizes the vehicle's ability to adjust its optimal operation strategy to unforeseen events.

The event handling mechanism is crucial for interpreting the dynamics involved in the vehicle's stopping process, taking into account both spatial and temporal elements to enhance the control strategy's responsiveness to real-world events.

V. REAL-TIME CONTROL

All nonlinear and mixed-integer optimizations are covered by the offline optimization using DP. Consequently, real-time control of the refrigeration system in the vehicle only needs to secure accurate tracking of the pre-computed trajectory in the presence of disturbances. A two-degree-of-freedom controller is therefore chosen as illustrated in Fig. 5.

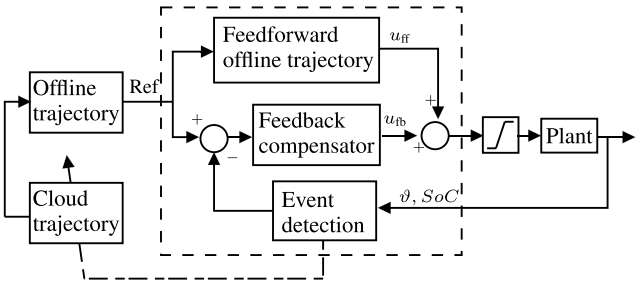

FIGURE 5. Real-time control block diagram with event detection.

The offline trajectory is downloaded to the delivery vehicle. The reference values for compressor n_{cpr} and fan s_{fan} are fed into the feedforward path. In the feedback loop a standard discrete Proportional-Integral-Derivative (PID) controller calculates the control signal u_{fb} as follows:

$$\boldsymbol{u}_{\text{fb}}(k) = K_p^u e^u(k) + K_p^y e^y(k) + K_i \sum_{i=0}^{N} e^y(i) T_s + K_d \frac{e^y(k) - e^y(k-1)}{T_s} \tag{27}$$

where $\boldsymbol{u}_{\text{fb}}(k)$ denotes the feedback control signal and $e^y(k) = y_s - y_s^{\text{ref}}$ is the error signal. In the same way

$e^u(k) = u_s - u_s^{\text{ref}}$ represents the deviation of the control signal u_s from its reference value u_s^{ref}. The controller gains K_p^y, K_p^u, K_i, and K_d define the closed-loop dynamics.

Furthermore, compressor speed constraints are implemented by Eq. (28):

$$n_{\text{cpr}}^{\text{ref}}(k) = \max\left(n_{\text{cpr}}^{\min}, \min\left(n_{\text{cpr}}^{\max}, \tilde{n}_{\text{cpr}}^{\text{ref}}(k)\right)\right). \tag{28}$$

A suitable integrator anti-windup mechanism is also employed. In Fig. 5 an event detection mechanism is used to continuously monitor the differences between the offline solution and the actual system outputs. As mentioned before, the event-handling process will be triggered if the specified hysteresis threshold for the deviation is exceeded.

VI. CONTROL FOR COMPARISON

In this section, alternative control strategies used for comparison are shortly described.

A. RULE-BASED CONTROL

The heuristic strategy, referred to as RB within this work, is designed to be of minimal complexity while managing fan switching to charge and unload the thermal storage in the secondary loop. The RB strategy employs a rule-based hysteresis proportional–integral controller, which represents an advanced industrial standard compared to the simple on–off controllers still commonly used in many commercial mobile refrigeration applications.

To ensure a fair comparison, the RB controller is also provided with predictive route information, such as disturbances over the same horizon length, N. The binary state of the fan s_{fan} is defined as ON $\rightarrow$ 1 or OFF $\rightarrow$ 0. The switching rules are defined by:

$$s_{\text{fan}}(k) = \begin{cases} 0 & \text{if } (\exists i \in \{1, 2, \ldots, n\} : N_i = 1) \\ & \vee\ s_{\text{door}} = \text{open}, \\ 1 & \text{if } (\vartheta_{\text{cc}_{|\min}} < \vartheta_{cc} < \vartheta_{\text{cc}_{|\max}}) \\ & \vee\ (\vartheta_{\text{gly}} < \vartheta_{\text{gly}_{|\min}}) \\ & \wedge \neg(\exists i \in \{1, 2, \ldots, n\} : N_i = 1) \\ & \wedge\ s_{\text{door}} \neq \text{open}. \end{cases} \tag{29}$$

Compressor speed n_{cpr} is determined by a conventional discrete PID controller:

$$n_{\text{cpr}}(k) = K_p e^y(k) + K_i \sum_{i=0}^{k} e^y(i) T_s + K_d \frac{e^y(k) - e^y(k-1)}{T_s} \tag{30}$$

Additionally, saturation of the control signal and anti-windup are implemented.

B. MIXED-INTEGER MPC

Model Predictive Control (MPC) is an effective control strategy that employs a model of the system to forecast future outputs. It determines the best control actions by minimizing a quadratic cost function over a limited horizon, incorporating elements of future inputs, outputs, and disturbances. For additional information, refer to [50].

1) RECEDING HORIZON MPC

The MPC formulation used here is based on prior results [21], [27], but utilizing a mixed-integer framework, revising the cost function, and incorporating the vehicle model. In contrast to [27] the non-linearity of the system model presented in Section IV is taken into account in the control design. In order to cover the non-linear nature of the system, successive linearization is applied to the model described in (18) using the Taylor series expansion at an operating point.

$$\dot{\tilde{x}} = f(\tilde{\boldsymbol{x}}, \tilde{\boldsymbol{u}}, \tilde{\boldsymbol{z}}), \tilde{y} = h(\tilde{\boldsymbol{x}}, \tilde{\boldsymbol{u}}, \tilde{\boldsymbol{z}})$$

where $\tilde{\boldsymbol{x}}, \tilde{\boldsymbol{u}}, \tilde{\boldsymbol{z}} \in \mu_0$ describe the current operating point.

For each time step k, the dynamics of the nonlinear system are approximated by linear models characterized by the Jacobians $A_{k|k}$ and $B_{k|k}$ $E_{k|k}$:

$$\begin{aligned} A_k &= \left.\frac{\partial f\ (x_k, u_k, z_k)}{\partial x_k}\right|_{\mu_0 = \tilde{x}, \tilde{u}, \tilde{z}} \\ B_k &= \left.\frac{\partial f\ (x_k, u_k, z_k)}{\partial u(k)}\right|_{\mu_0 = \tilde{x}, \tilde{u}, \tilde{z}} \\ E_k &= \left.\frac{\partial f\ (x_k, u_k, z_k)}{\partial u(k)}\right|_{\mu_0 = \tilde{x}, \tilde{u}, \tilde{z}} \\ d_k &= f(\tilde{x}, \tilde{u}, \tilde{z}) - A_k \tilde{x_k} - B_k \tilde{u_k} - E_k \tilde{z_k}. \\ g_k &= h(\tilde{x}, \tilde{u}, \tilde{z}) - C_k \tilde{x_k} \end{aligned} \tag{31}$$

where $C_k = [1\ 0\ 0\ 0]$ and $k \in \mathbb{N}^+$.

The resulting Jacobian matrices are discretized using the exponential matrix method e^{AT_s}, with a sampling time of T_s. The matrices are calculated based on the current state and control input in order to provide a locally linear representation of the nonlinear dynamics. This allows for the approximation of dynamic behavior by a linear time-varying (LTV) model, [51], [52]. By appropriately extracting the system matrices A_k, B_k, and E_k as well as the equilibrium offset terms d_k and g_k, one obtains the linear time-invariant system:

$$\begin{aligned} x_{k+1|k} &= A_{k|k} x_{k|k} + B_{k|k} u_{k|k} + E_{k|k} z_k + d_{k|k} \\ y_{k+1|k} &= C_{k|k} x_{k|k} + g_k. \end{aligned} \tag{32}$$

The predicted output can be expressed in matrix form, obtained along the sequence of operating points as follows:

$$\hat{\boldsymbol{Y}}(k) = \boldsymbol{F}\boldsymbol{x}(k) + \boldsymbol{\Phi}_u \boldsymbol{U}(k) + \boldsymbol{\Phi}_z \boldsymbol{Z}(k),$$

where the matrices $\boldsymbol{F}$, $\boldsymbol{\Phi}_u$ and $\boldsymbol{\Phi}_z$ are computed as:

$$\hat{\boldsymbol{Y}}(k) = \begin{bmatrix} \hat{y}(k+1|k) \\ \hat{y}(k+2|k) \\ \vdots \\ \hat{y}(k+N|k) \end{bmatrix}, \boldsymbol{U}(k) = \begin{bmatrix} \tilde{u}(k) \\ \tilde{u}(k+1) \\ \vdots \\ \tilde{u}(k+N-1) \end{bmatrix}$$

$$\boldsymbol{F} = \begin{bmatrix} \tilde{C}\tilde{A} \\ \tilde{C}\tilde{A}^2 \\ \vdots \\ \tilde{C}\tilde{A}^N \end{bmatrix}$$

$$\Phi_i = \begin{bmatrix} \tilde{C}\tilde{B}_i & \cdots & 0 \\ \tilde{C}\tilde{A}\tilde{B}_i & \cdots & 0 \\ \vdots & \cdots & \vdots \\ \tilde{C}\tilde{A}^{N_p-1}\tilde{B}_i & \cdots & \tilde{C}\tilde{A}^{N_p-N_p}\tilde{B}_i \end{bmatrix}$$

where $i \in \{u, z\}$.

The predictive control variables are computed by minimizing the cost function J_{MPC} with the reference signal y_k^{ref} over the prediction horizon; see Eq. (33).

$$J_{\text{MPC}}(\boldsymbol{u}_k, \boldsymbol{x}_k, \boldsymbol{z}_k) = \|\delta_{\text{cc}}\|_{Q_1}^2 + \|\delta_{\text{gly}}\|_{Q_2}^2 + \sum_{k=0}^{N-1} \|y_k - y_k^{\text{ref}}\|_{Q_3}^2 + \|u_k\|_{R_{1,2}}^2 + \|z_k\|_{R_3}^2 - \|SoC_k\|_{Q_4}^2 \quad (33)$$

The objective is then to determine the control vector $u = [u, \ldots, u_N]$ in such a way that an error function between the set-point and the predicted output is minimised and simultaneously satisfying the constraints. δ_{gly} and δ_{cc} are slack variable to utilise soft constraints. The MI-MPC is a special case of MPC, where an input can only adopt integer values (s_{fan}).

$$\min_{u_s, \ldots, u_{s+N}} \quad J_{\text{MPC}}(\boldsymbol{u}_k, \boldsymbol{x}_k, \boldsymbol{z}_k) \quad (34a)$$

$$s.t. \quad x_{k+1} = \boldsymbol{A}_k\boldsymbol{x} + \boldsymbol{B}_k\boldsymbol{u} + \boldsymbol{E}_k\boldsymbol{z} + \boldsymbol{d}_k \quad (34b)$$

$$n_{\text{cpr}_{|\min}} \leq n_{\text{cpr}_{|k}} \leq n_{\text{cpr}_{|\max}} \quad (34c)$$

$$\vartheta_{\text{cc}_{|\min}} - \delta_{\text{cc}} \leq \vartheta_{\text{cc}_{|k}} \leq \vartheta_{\text{cc}_{|\max}} + \delta_{\text{cc}} \quad (34d)$$

$$SoC_{\min} \leq SoC_k \leq SoC_{\max} \quad (34e)$$

$$\vartheta_{\text{gly}_{|\min}} - \delta_{\text{gly}} \leq \vartheta_{\text{gly}_{|k}} \quad (34f)$$

$$x_0 = x_k \quad k \quad (34g)$$

$$s_{\text{fan}} \in \{0, 1\} \in \mathbb{U} \quad (34h)$$

$$\delta_{\text{cc}} \geq 0, \quad \delta_{\text{gly}} \geq 0$$

$$Soc_k, \vartheta_{\text{cc}}, \vartheta_{\text{gly}} \in \mathcal{X}$$

$$\forall k = 0, \ldots, N-1 \quad (34i)$$

The specific implementation to compute the mixed-integer quadratic programming (MIQP) problem at each discrete-time step using the branch and bound (B & B) algorithm made use of the Gurobi solver [53] and CasADi toolbox [54].

2) SHRINKING HORIZON MPC

Classical MPC design uses a receding horizon of constant length, providing consistency and robustness for various control tasks. Alternatively, the horizon may extend to the end of a given trajectory, therefore shrinking as time progresses. As demonstrated by [55], it can be sufficient to design a shrinking horizon suitable for reaching a destination optimally.

We decompose the problem formulation into sub-problems and apply shrinking horizon MI-MPC iteratively, significantly reducing the computational complexity. In addition to the optimal control formulations from, the shrinking horizon MI-MPC is illustrated in the following:

$$\begin{aligned} \min_{u,T} \quad & J(\boldsymbol{u}_k, T; \boldsymbol{x}_k) = J_{\text{MPC}}(\boldsymbol{u}_k, \boldsymbol{x}_k, z_k) + T + Q_5\delta_h^2 \\ \text{s.t.} \quad & \text{eq.(34}b\text{)} \\ & \text{eq.(34}c\text{)} - \text{eq.(34}i\text{)} \\ & T + \delta_h = N \times T_s, \\ & \delta_h \geq 0 \\ & x(T) = x_{\text{ref}} \\ & \forall k = 0, \ldots, N-1 \end{aligned}$$

In this optimization problem next to the optimal control input u an optimal predictive horizon T is obtained. The objective function is also extended by a slack variable δ_h which is relaxing the strict additional constraint on the horizon length. The included term $Q_5\delta_h^2$ penalizes significant deviations from the desired horizon length.

VII. SIMULATION RESULTS

In this Section, the proposed approach is analyzed and compared with several real-time strategies, including mixed-integer shrinking and constant-receding model-based controllers, and an enhanced rule-based strategy, across two real-world driving cycles used in delivery of cooled goods. First, the simulation setup is presented and the objectives of the delivery cycle are given to assess the hierarchical approach. This is followed by a performance evaluation against other control strategies, as outlined in Section VII-D. The results reported in this section refer to simulations performed using Matlab R2023a on a computer with 2.7 GHz of base CPU speed and 32 Gb of RAM.

A. MODEL PARAMETERS

This study's simulation of a real-world driving cycle includes a refrigeration-modified e-NV200 small truck, depicted in Fig. 6, with a nominal power of 80 kW and a battery capacity of 40 kWh [56].

Various driving cycles, like the a Worldwide harmonized Light vehicles Test Cycle (WLTC) or Real Driving Emissions (RDE), have been used to ascertain the power train and battery parameters, which parameterize the vehicle and battery models. The values for longitudinal driving resistance were obtained through a coasting measurement and can be found in Table 1. The vehicle's measurement data, along with the state of charge, were aligned using a polynomial model through the common least squares fitting technique [57]. The

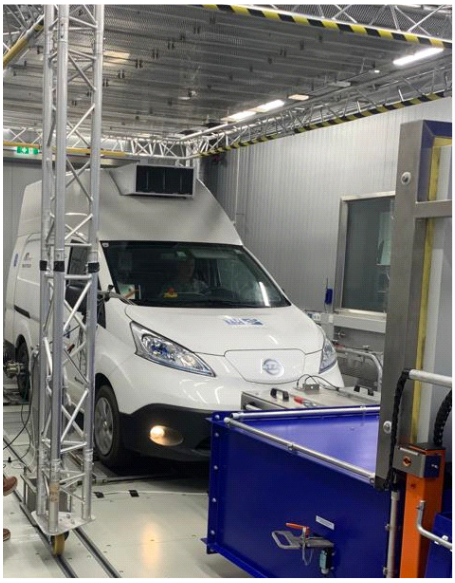

FIGURE 6. Experimental testbed with refrigerator truck. The air temperature at the measurement testbed can be regulated to remain constant at $\vartheta_{\text{amb}} = -5°\text{C}$, 23°C and 30°C.

outcome of this parameterization is shown in the subsequent figure.

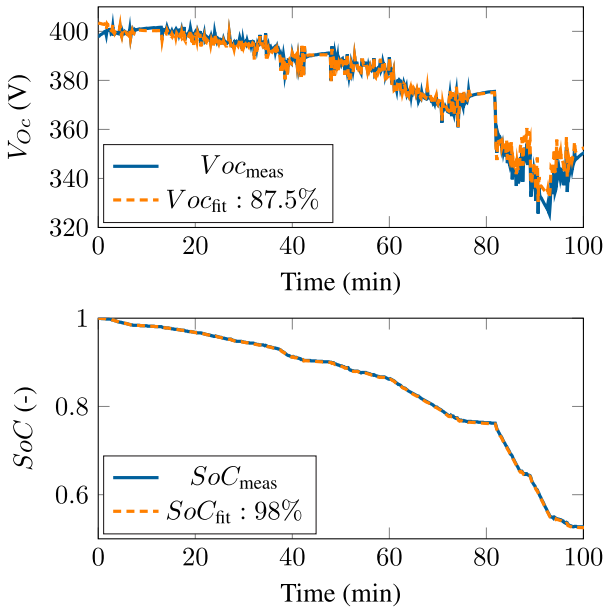

FIGURE 7. Testbench WLTC measurements and evaluation of battery model at $\vartheta_{\text{amb}} = 23°\text{C}$. Top: Comparison to measurement and fit of open circuit voltage (V_{OC}) model. Bottom: Comparison to measurement and fit of state of charge (SoC) model.

As illustrated in Fig. 7, an excellent match is achieved between model and measurements. The upper graph shows the actual open circuit voltage, denoted as $V_{OC_{\text{meas}}}$, with the fitted voltage model, $V_{OC_{\text{fit}}}$, achieving an 87.5% fit. The lower graph displays the comparison of the measured State of Charge (SoC_{meas}) against the fitted model (SoC_{fit}), demonstrating a high fidelity of 98% to the measured data. In this study, we do not investigate the validation of the model of the cooling chamber since this is shown in [21]. For sake of completeness, all system parameters of the modeled cooling system are listed in the appendix, see Table 4. The specific parameters for the battery, control-related system limitations, and vehicle model can be found in Table 1.

TABLE 1. Simulation parameters.

Symbol	Value	Parameter
A_v	3.36 m^2	Vehicle frontal area
g	9.812 m/s^2	Gravitational acceleration
μ	$1.3 \cdot 10^{-3}$	Rolling friction coefficient
c_r	0.35	Drag coefficient
ρ_{air}	1.2 kg/m^3	Air density
C_0	123.61 N	Constant vehicle coefficient[a]
C_1	2.6395 N/(km/h)	Linear vehicle coefficient[a]
C_2	0.0543 $\text{N}^2/(\text{km/h})^2$	Quadratic vehicle coefficient[a]
$P_{v,\max}$	80 kW (109 PS)	Vehicle power
Q_{nom}	52 kWh	Nominal charge battery capacity
$P_{b,\max}$	8.9 kW	Max power
R_0	0.08 Ω	Internal resistance
$a_{1,2,3,4}$	8.3 , 25.7 , 50.5, 318.3	Open-circuit voltage
$\eta_{\text{ch,dis}}$	0.85, 0.87	Efficiency

h = hour, s = second, W = Watt, m = meter, Ω = Ohm, N = Newton, kg = kilogram.
[a] according to experiments.

B. SELECTION OF DRIVING CYCLES

The two driving cycles under investigation were selected to represent typical delivery routes which start at a logistic center, lead into the urban area with multiple stops, and lead out of the city to end at the logistic center. The relative positive acceleration (RPA $= \frac{\int v \cdot a^+ \, dt}{\int v \, dt}$) was used to assess each cycle's suitability. In [58] a high correlation between RPA and energy consumption in battery electric vehicles was suggested. The first cycle had an RPA of 0.23 m/s^2, indicating urban driving with heavy traffic and a medium climb. The second cycle had an RPA of 0.4 m/s^2, representing sub-urban driving with a significant elevation profile. Both cycles are shown in Fig. 8. The cycles contain between ten and fourteen delivery stops, lasting in average 60 seconds with 8-20 seconds door openings each. The average duration of the mission was 2.5 hours of driving, with an average distance traveled of 90 km and an average speed of 35km/h. We utilized AVL Route Studio to create realistic driving cycles for delivery routes using a sampling time of 1 second. The environmental conditions are based on weather data from Vienna ($\overline{\vartheta}_{\text{amb}} = 23.8°\text{C}$) and Salzburg ($\overline{\vartheta}_{\text{amb}} = 21.2°\text{C}$) from June to August to cover the worst-case scenario [59].

The characteristics of the two driving cycles are detailed in Fig. 8. The upper graph shows the vehicle's speed and corresponding elevation, while the second graph depicts electrical power and door opening times.

The results of the presented control strategy are shown in detail for the first driving cycle in Fig. 9. The sampling distance is $\Delta s = 20\text{m}$, and the reference temperature of the cooled compartment is 1 °C centigrade with a temperature

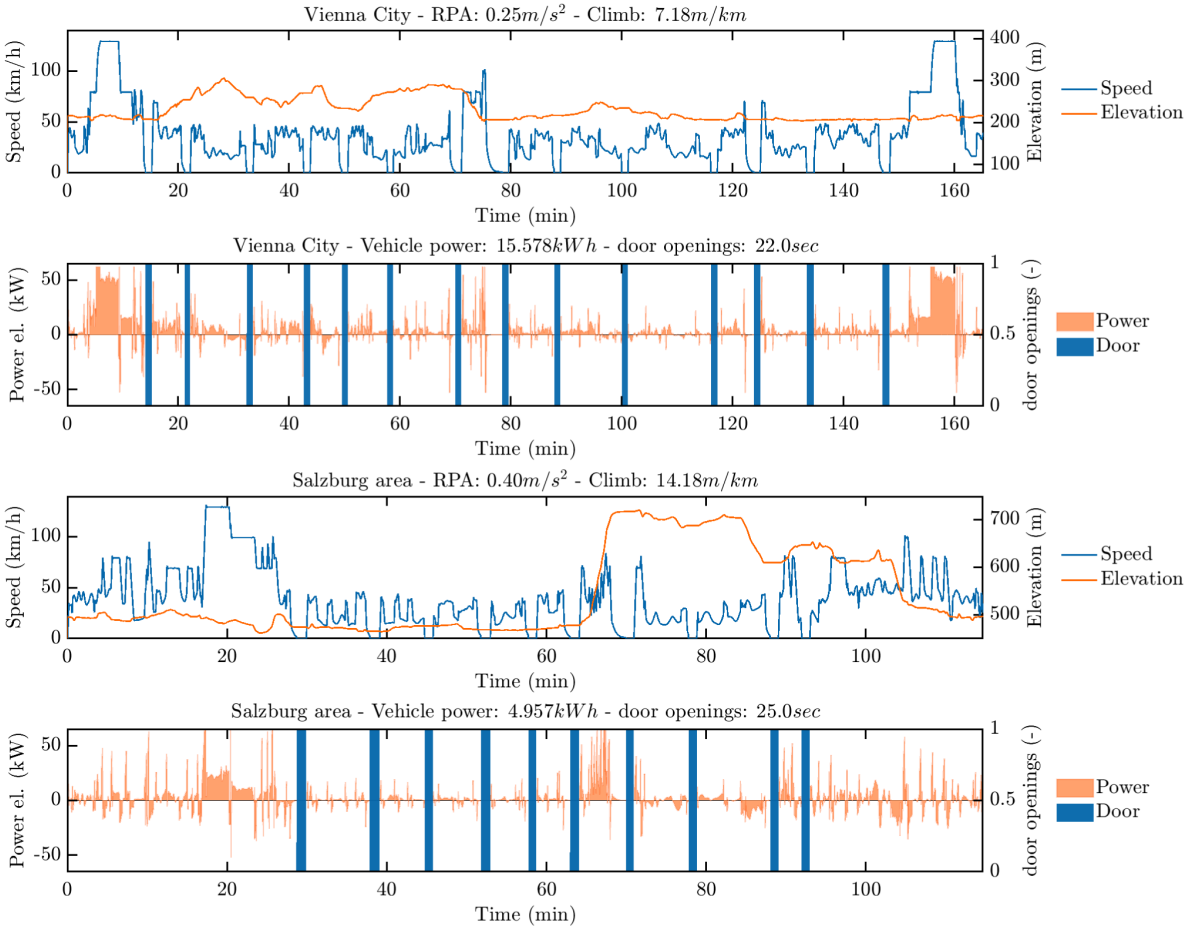

FIGURE 8. **Showing the speed and elevation profiles of example driving cycles, including power distribution and delivery stops during the driving scenarios.**

window of $\Delta\vartheta = 1°C$. The temperatures of the system $\vartheta_{cc}, \vartheta_{gly}, \vartheta_{w}$ during the complete driving cycle are shown in the upper graph. Given that the primary control objective is to compensate the impact of door openings and maintain the box temperature ϑ_{cc} within the specified temperature range, it is reasonable to concentrate on the behavior during disturbances. In the graph provided in Fig. 9, the focus is placed on the intervals between 25.4 km and 26.6 km, as well as 63.4 km and 64.6 km.

The left column in Fig. Fig. 9 depicts a door opening that lasts for 19 seconds, while the right right column shows results for a door opening that lasts for 16 seconds. The top row depicts the temperatures for the full delivery cycle.

The second row of the figure provides a detailed overview of the controlled temperatures. This demonstrates that the control strategy applies a predictive storage method in the thermal storage (water-glycol storage) prior to a door opening. Before any door opening occurs, this approach guarantees that the temperature in the glycol water storage ϑ_{gly} is charged within the permissible temperature limits of the water pump, which are represented by the constraint of ϑ_{gly}. The controlled temperature inside the refrigerated truck ϑ_{cc} is maintained within the required range, except for the duration of the door openings. These results are achieved through predictive fan switching and simultaneous optimal compressor control, as depicted in the last two rows of Fig. 9.

The third row of the Figure displays the *SoC* of the system, and the fourth row shows the durations of the door openings.

C. CONTROLLER TUNING FOR COMPARISON

To ensure a fair performance comparison of different controllers, both rule-based and model-based strategies are evaluated. The following assumptions are made: i) All control techniques use the same initial conditions. ii) The a state-of-the-art configuration of the controller is used for each controller. iii) The performance of the controllers is evaluated for the disturbance response of the door openings. The Tuning of control parameters significantly impacts the controller's performance and accuracy. Therefore, in order to ensure a fair comparison of these controllers, we employ the same Genetic Algorithm (GA) optimizer to fine-tune these parameters. The goal is to evaluate the controllers' performances under the same tuning conditions.

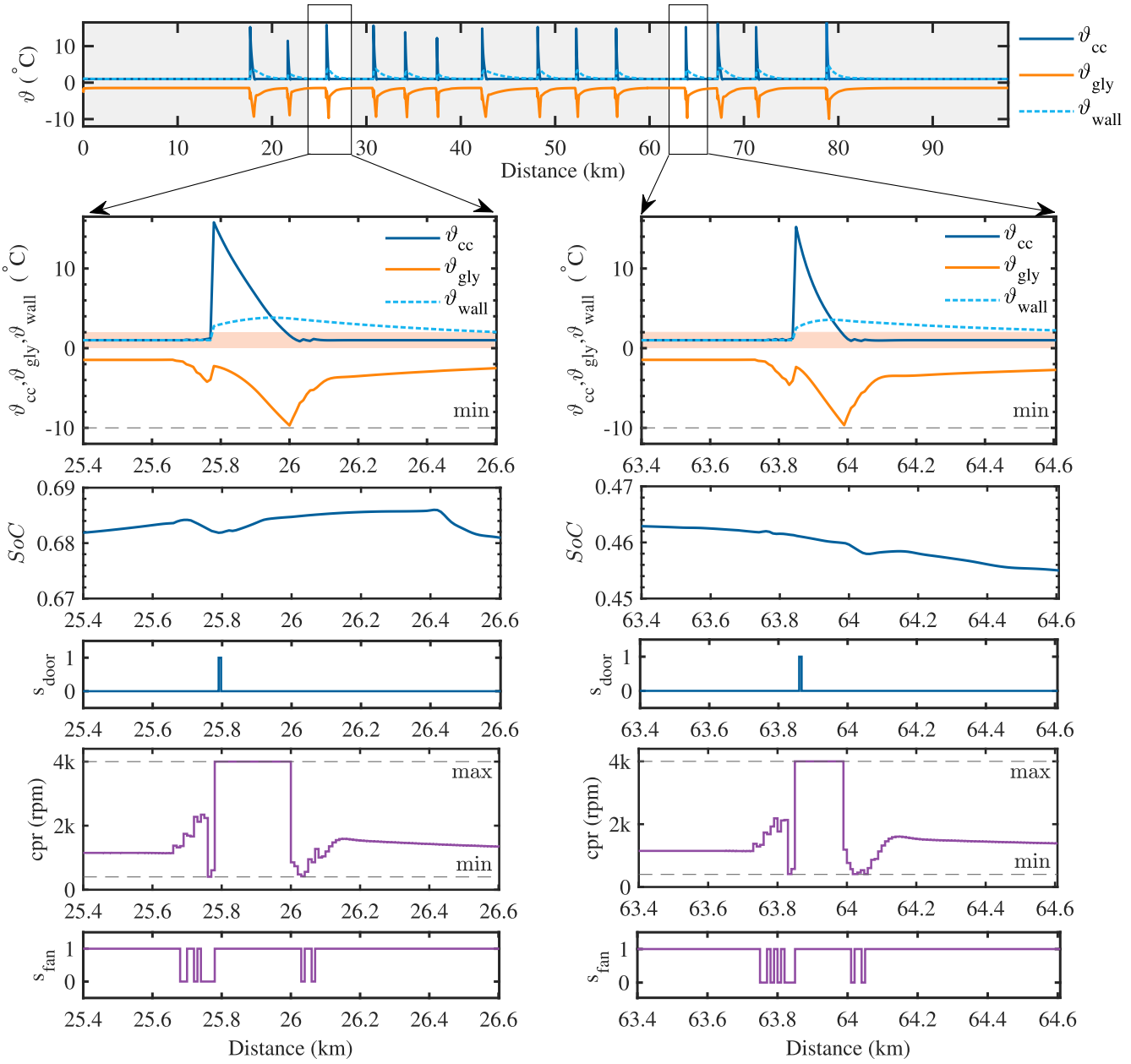

FIGURE 9. Performance of the multi-hierarchical control approach during the first driving scenario, emphasizing the thermal results of the proposed control strategy and detailed views of two disturbance events.

In the GA the following criteria are evaluated:

$$\text{maximum error: } \varepsilon_{\vartheta_{\max}} = \max_{t\in[0,T]} |\varepsilon_d(t)|$$

$$\text{average error: } \varepsilon_{\vartheta_{\text{RMS}}} = \sqrt{\frac{1}{T}\int_0^T \varepsilon_d(t)^2 \mathrm{d}t}$$

$$\text{settling time: } \varepsilon_{t_{\text{set}}} = \left|y(t') - y_{\text{T}}\right| \leq \epsilon \cdot |y_{\text{T}}| \; \forall t' \geq t$$

with $t > 0$ and T defines the gap between the disturbances. ε_d presents the deviation from the reference value $y(t)$ and $y(T)$ defines the steady value at the end of the gap. Transients should decay to within a specified small percentage of $y(T)$ and remain in that range, typically around $\epsilon = 5\%$. The following cost function is utilized for the GA optimization:

$$J_{\text{GA}} = \varepsilon_{\vartheta_{\max}} + \varepsilon_{\vartheta_{\text{RMS}}} + \varepsilon_{t_{\text{set}}} \tag{35}$$

A population size of 150 and a maximum of 100 generations are used. The resulting optimized parameters can be found in Table 2. Furthermore, for the rule-based and MI-MPC approaches, a prediction horizon of N=30 is used, with a sampling distance of 20 m. For MI-SHMPC, an initial horizon of N=200 is employed to maintain a reasonable computational time. An explanation of the horizon length will be provided in Section VII-D4.

The weights for the offline solution compare Section IV-B2 are chosen to Q_1=100 and $Q_{2,3}$=10, for state window, are chosen to $Q_{4,5}$=200 and for boundaries $Q_{6,7} = 200$ and for the terminal costs $Q_{8,9} = 50$. The hard constraints are defined according to the limitations of the system as shown in Table 1.

TABLE 2. Parameter values for the real-time controllers.

Control technique	Optimized parameter values
MH-Opt	$K_p^u = 1.243$, $K_p^y = 5.056$, $K_i = 1.105$, $K_d = 0.418$
Rule-based	$K_p^y = 5.050$, $K_i = 1.4183$, $K_d = 0.3049$
MI-SHMPC	$Q_1 = 1.2$, $Q_2 = 50$, $Q_3 = 175.5$, $Q_4 = 1.5$, $Q_5 = 3.3$, $R_1 = 12$, $R_2 = 3$, $R_3 = 12$
MI-MPC	$Q_1 = 1.15$, $Q_2 = 30.5$, $Q_3 = 200.5$, $Q_4 = 0.8$, $R_1 = 10$, $R_2 = 4$, $R_3 = 10$

D. PERFORMANCE COMPARISON

1) COMPARISON FOR DOOR OPENING

Fig. 10 illustrates a comparative analysis of four distinct control strategies: MH-Opt, RB, MI-SHMPC, and MI-MPC, across a distance before and after a door opening (from 21.2 km to 22.2 km). The analysis is based on various performance metrics and operational constraints, with a particular focus on temperature deviation.

In the upper graph of Fig. 10, the temperature in the cooling chamber (ϑ_{cc}) resulting from the door opening is shown for each control strategy over the specified distance. Initially, all strategies follow a similar trend of utilizing thermal storage in the water-glycol cycle before the disturbance occurs. The RB strategy comes close to the maximum temperature constraint, while the MH-Opt strategy significantly loads the thermal storage by controlling the compressor speed, as depicted in the second and third graphs. The MI-SHMPC strategy utilizes the thermal storage slightly more and achieves a faster steady state compared to MI-MPC. Both strategies employ a model-based approach and require more control effort of the compressor, especially after the disturbance, as evident in the third graph. The results in Fig. 10 confirm the effectiveness and suitability of all control strategies without violating state and input constraints. Further analysis of the simulation data will show the advantages and disadvantages of these control strategies.

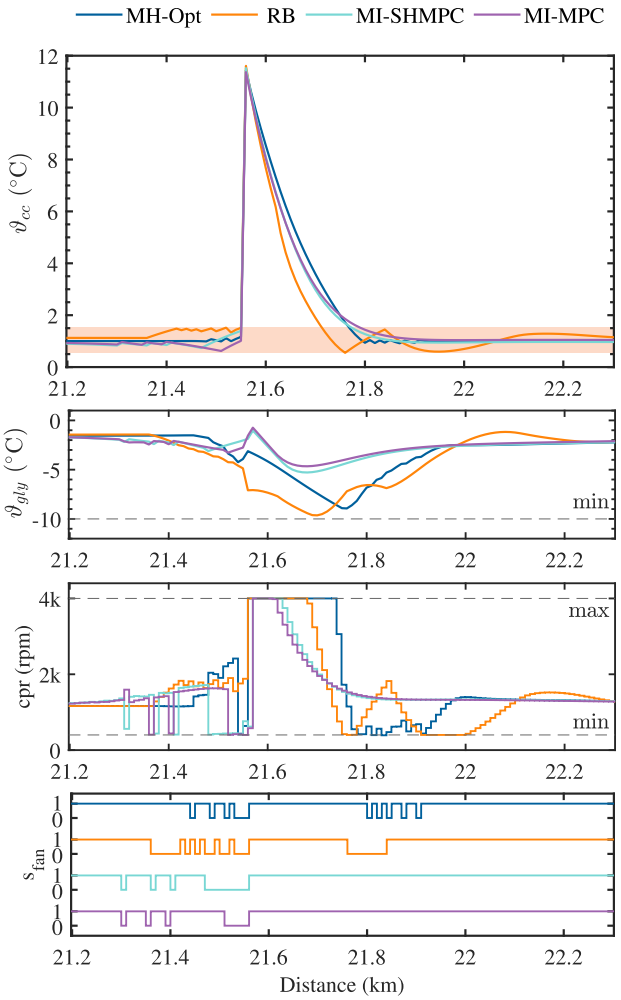

FIGURE 10. Performance comparison: Temperature of the cooling chamber, glycol temperature, compressor speed, and switching behavior.

2) COMPARISON BASED ON PERFORMANCE INDICATORS

Fig. 11 shows a comparative analysis of the different control strategies (MH-Opt, Rule-based, MI-SHMPC, and MI-MPC) in three performance metrics: error, overshoot, and settling time in the two distinct delivery cycles of Fig. 8, denoted cycle 1 and cycle 2.

The first box-plot in Fig. 11 displays output errors in degrees Celsius for each control method. Especially the RB-control shows large variations. Although it mostly stays within the acceptable temperature limit, it shows a significantly higher error compared to the other methods. The MH-Opt method consistently maintains a lower range of errors across both cycles, showing a 10-fold improvement in lower error and, therefore, less deviation from the target temperature. Compared to MI-SHMPC and MI-MPC, the error is 1.2 to 2.8 times smaller. The results of the predictive methods are within the required boundaries, even if some values touch the limits.

The second box-plot compares overshoot, which is crucial in systems where lower temperatures can lead to damage to goods. Once again, during cycle 1, the Rule-based method exhibits significant overshoot compared to other methods. This is due to the simple hysteresis-based switching, making it challenging to achieve predictive switching and a globally optimal solution. There are no significant differences visible between the two advanced control strategies.

The third box-plot illustrates the settling time in seconds, which measures how quickly the system returns to a steady state within the temperature window after a door opening. Shorter settling times are generally preferred. The plots show that the MH-Opt yields similar results to advanced model predictive methods, offering faster settling times compared to the rule-based strategy. Although the distribution over the cycle appears to be lower for the MH-Opt method, the

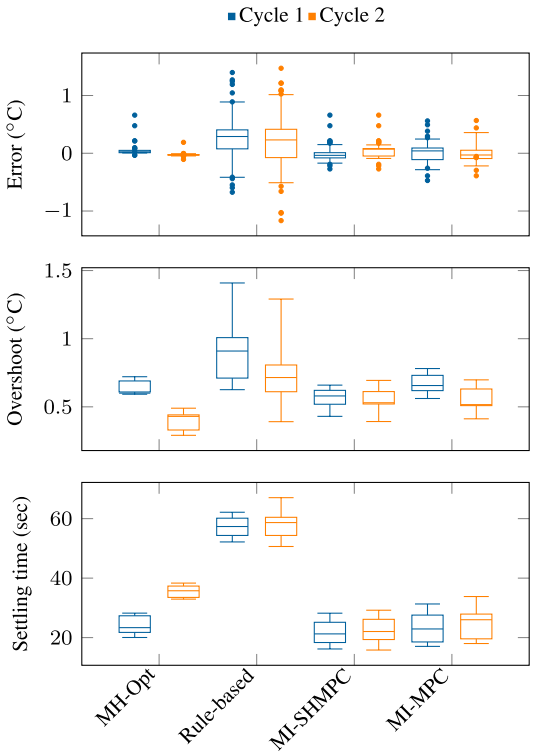

FIGURE 11. Performance evaluation online strategy. Error, overshoot and settling time.

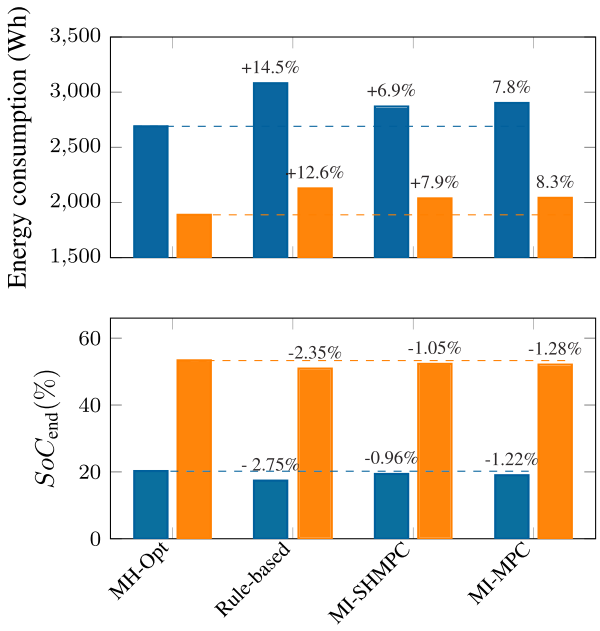

FIGURE 12. Comparison of energy consumption and *SoC* end value for all control strategies and for each driving cycle (**blue:** *cycle 1* where MH-Opt: 27.26 Wh/km, RB:31.21 Wh/km, MI-SHMPC: 29.07 Wh/km, MI-MPC: 29.40 Wh/km; **orange:** *cycle 2* where MH-Opt: 26.85 Wh/km, RB: 30.24 Wh/km, MI-SHMPC: 28.96 Wh/km, MI-MPC: 29.03 Wh/km).

MI-SHMPC settling process achieves an even smaller settling time.

Fig. 11 clearly shows that MH-Opt control consistently displays strong performance across different driving missions. Furthermore, advanced mixed-integer model-based control strategies show similar results with some insignificant advantages.

3) COMPARISON BASED ON ENERGY CONSUMPTION INDICATORS

Fig. 12 provides an analysis of the four control strategies in terms of their energy usage metrics. In the top plot, the bar graphs illustrate energy consumption in watt-hours (Wh), with each bar accompanied by a percentage indicating the increase in energy consumption compared to the MH-Opt approach. It is evident that MH-Opt exhibits the lowest energy usage. In contrast, the RB control shows an excess consumption of 12.6% to 14.5%, even though the primary focus of MH-Opt was optimal control performance. The MI-SHMPC and MI-MPC exhibit a smaller excess consumption of 6.9% to 8.3%. The advantage of the shrinking horizon over the receding horizon approach with a constant window size is not significant.

The bottom plot of Fig. 12 is another representation of these results. It shows a bar graphh of the *SoC* at the end of the delivery cycle. Again, deviations from the results of MH-Opt are given in percentages, absolute values are given in the caption.

4) COMPARISON BASED ON COMPUTATION TIME

Fig. 13 illustrates the computational time for each control strategy for delivery cycle 1. The red dashed line represents the worst-case limit within which a feasible optimal solution must be found. If this limit is exceeded, either a sub-optimal or a fallback solution would have to be utilized, respectively. Note that the numbers were achieved using a computer with multi-core processor running at 2.7GHz.

From the upper plot of Fig. 13 shows the average computational limit where it becomes evident that the MH-Opt and RB methods have an almost negligible computational time of less than 0.01 seconds, ensuring real-time capability throughout the entire driving scenario. This is further supported by the computational time over the total travel distance in the lower plot of Fig. 13 that shows a spatial-dependent computational limit.

The MI-SHMPC reduces computational time with reduced horizon. However, until 20 km the computational effort is too large for real-time application. Violations of the computational time limit also occur during disturbances for both model-based approaches.

5) SENSITIVITY ANALYSIS

This section examines the impact of uncertainties on energy consumption and temperature regulation. The robustness of the proposed approach is evaluated by varying both environmental conditions and model parameters. Given the approximations inherent to the complex DP optimization employed, empirical comparisons are reasonable for a sensitivity analysis.

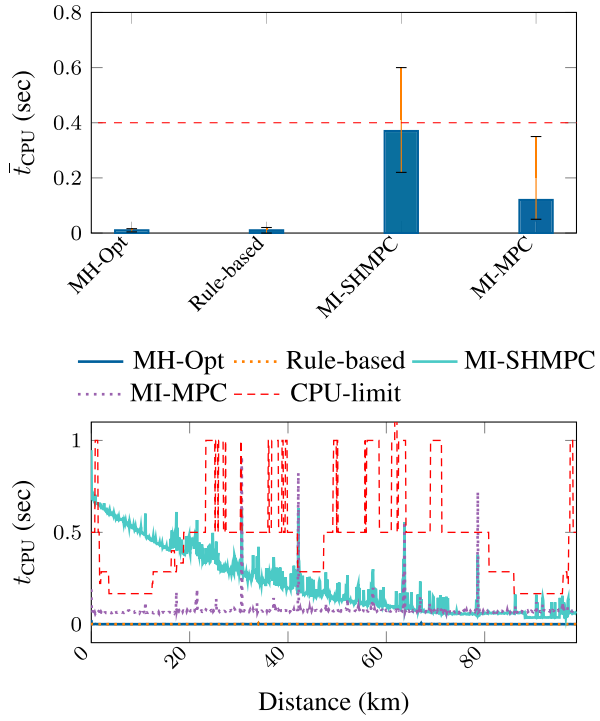

FIGURE 13. Computational time $\bar{t}_{CPU}$ of different control strategies. Top: Computational time in average mean time. Bottom: computational time t_{CPU} over distance of cycle 1. Simulation setup: MATLAB R2023a, CPU speed 2.70 GHz, and 32.0 GB of RAM.

Model parameters of the simulation model are chosen differently from those used in control design. Specifically, parameters/inputs are varied by ± 10%, and the corresponding results are presented in Table 3. The magnitude of variation is chosen such that it no events are triggered (see IV-C).

TABLE 3. Analysis of sensitivity with respect to input and parameter uncertainties, respectively.

	MH-Opt		RB		MI-SHMPC		MI-MPC	
	E (Wh)	MAE (°C)	E (Wh)	MAE (°C)	E (Wh)	MAE (°C)	E (Wh)	MAE (°C)
BASELINE								
	2690.6	0.02	3081.1	0.31	2869.9	0.05	2902.2	0.09
ENVIRONMENTAL UNCERTAINTIES								
+10% P_V	2699.7	0.12	3035.5	0.37	2794.9	0.05	2897.6	0.10
-10% P_V	2689.4	0.09	3081.3	0.33	2869.1	0.03	2921.2	0.07
+10% ϑ_{amb}	2786.1	0.20	3144.3	0.49	2937.1	0.05	2972.5	0.09
-10% ϑ_{amb}	2610.5	0.15	3054.9	0.44	2800.2	0.06	2882.3	0.09
MODEL UNCERTAINTIES								
+10% ζ_1	2671.1	0.20	3078.3	0.37	2869.2	0.09	2910.1	0.12
-10% ζ_1	2728.3	0.17	3103.6	0.49	2870.1	0.11	2912.3	0.15
+10% ξ_1	2649.1	0.13	2872.1	0.41	2820.8	0.08	2892.5	0.12
-10% ξ_1	2705.1	0.22	3059.5	0.38	2943.7	0.10	2952.6	0.13

MAE = Mean Absolute Error, E = Energy

Table 3 displays energy consumption sensitivity for the refrigeration unit (E) and the mean absolute error (MAE) of the controlled cargo room temperature ϑ_{amb} for different control methods under standard and uncertain conditions. The MH-Opt approach maintains competitiveness with MPCs despite minor losses in optimality. It ensures robustness by recalculating in response to significant uncertainties and identifies deviations through *SoC* monitoring. The RB controller is significantly more sensitive to the given variations.

VIII. DISCUSSION

Overall, the MH-Opt approach demonstrates excellent performance, as shown in Fig. 10, Fig. 11 and Fig. 12. It can compete with other state-of-the-art control strategies for thermal plants with thermal storage in terms of energy savings, without the need for hardware adaptations on-board the vehicle. MH-Opt is well-suited for reducing both energy costs and loss of goods due to temperature violations in applications of refrigeration vehicles. The hierarchical approach uses a dynamic programming (DP) algorithm for offline optimization, allowing for a theoretically global optimal solution, which outperforms most heuristic methods in this matter. Unlike MPC, the DP algorithm offers simple and flexible integration in discretization through adaptive grid sizing, compare [49]. Additionally, a cost-to-go matrix triggered by specific events is employed, a feature not typically found in MPC formulations. Rule-based methods are commonly used in the field of transport logistics. However, due to the complexity and nonlinearity of the system, achieving energy-optimal operation with heuristic rules can result in a complex and difficult to define rule set, particularly when considering multiple types of vehicles and refrigerated units.

Note that the presented approach achieves energy savings of approximately 12.6% to 14.5% compared to conventional control methods, and 6.9% to 8.3% compared to MI-SHMPC and MI-MPC. Although advanced predictive control schemes are considered state-of-the-art, they utilize a horizon that covers only part of the driving mission. For effective use of thermal storage with slower dynamics, a longer optimization horizon is advisable. However, shorter sampling rates are necessary to accurately describe door openings. Furthermore, the results of the MI-SHMPC indicate that further extension of the initial horizon is not feasible; see Fig. 13. Consequently, this leads to longer computation times or necessitates powerful hardware, which is not commonly found in current vehicles to leverage the potential of an MPC. In contrast, the DP optimization covers the entire remaining driving mission, leading to even better performance and lower energy consumption. This is mainly due to the optimal use of thermal storage throughout the entire driving mission, while still being able to react to door openings with smaller discretization steps.

This work is based on simulations that are parametrized with both real-world measurements and literature values. Nevertheless, a real-world implementation needs further investigation and adaptation. Large parameter uncertainties of the prediction models and the real-world system could be handled by either online parameter learning or a disturbance observer [60], [61] to adapt the prediction model for

offline reference calculation. In practical implementation, numerous uncertainties can be mitigated by recalculation of the offline solution, ensuring robustness under varying conditions. However, expertise is necessary to determine the optimal threshold that balances solution accuracy with the frequency of recalculation (triggered by events). It is also important to identify the upper limit of recalculations that could necessitate a reevaluation of the optimized route, taking into account changes in vehicle consumption estimates. The recalculation process is outsourced to the cloud, making this approach viable for vehicles with limited computational resources, as many logistic centers already use systems like GPS and internet connectivity for their fleets. Frequent recalculation may increase cloud activity and communication load, which can pose challenges for larger fleets. However, as cloud computing continues to improve, this constraint will likely be eliminated in the near future, enabling the practical application of this approach even for larger fleets. Although an event-based re-computation of the optimal trajectory is included in the proposed methodology, the effect of small disturbances along the mission will be detrimental to the performance. This is especially true if deviations always stay below the threshold value for triggering the re-computation. The quantification of the robustness to small but persistent disturbances will, therefore, be an important topic of future research.

Another challenge for larger fleets is the variation in characteristics of both the vehicles and the refrigeration systems. Identifying suitable models is required, similar to other model-based methods (e.g. MPC). This ultimately involves software adaptation without requiring hardware changes for different types of refrigeration systems or vehicles operating in different climates, allowing this approach to be scalable for larger fleets.

The potential energy savings per transport vehicle at the local level are quite promising, especially when viewed from a global perspective. Although not the main focus of this work, several studies have highlighted the global impact of CO2 emissions from refrigerated food transport, underscoring the growing importance of the approach presented here [62], [63], and [64].

IX. CONCLUSION

The research presented in this paper aimed to provide a globally optimal solution for the operation of a refrigeration system on a small electric delivery truck. An important economical constraint for such a solution is the compatibility with low-cost control hardware onboard the vehicle. The proposed solution consists of an offline optimization of the complete trajectory of the refrigeration system, which is computed prior to the delivery mission. This ensures global optimality for the nominal mission. In the case of unknown disturbances, only the less computationally intensive part of the optimization needs to be re-run.

This approach only requires a standard control hardware onboard the vehicle's refrigeration system (e.g. PID-control) together with a small memory for the optimized trajectory. Furthermore, a wireless connection to upload the position of the vehicle and internal states, and to download a new trajectory in the case of severe disturbances is required.

The implementation of the dynamic programming (DP) optimization algorithm can be flexibly chosen: A dedicated computing facility at the logistics center is equally feasible as a cloud-computing solution. This feature helps to set up a specific implementation of the proposed methodology.

In conclusion, the study validates that the proposed hierarchical optimization strategy is an efficient and cost-effective approach to managing temperature and energy in refrigerated electric transport under dynamic conditions and with limited hardware resources. This opens up opportunities for future research to investigate improvements in computational strategies and exploitation of environmental information to further enhance performance in real-world delivery applications.

APPENDIX.

A. ABBREVIATIONS

The following abbreviations are used in this manuscript:

DP	Dynamic programming.
GA	Genetic Algorithm.
MIQP	mixed-integer quadratic programming.
MPC	Model Predictive Control.
PID	Proportional-Integral-Derivative.
RB	Rule-Based.

B. PARAMETERS OF THE MODEL

In Table 4 the parameters for the model are shown.

TABLE 4. Model parameter values.

Symbol	Quantity	Units
α_1	$250 \cdot 10^{-6}$	$\mathrm{W\,rpm^{-1}}$
α_2	$1.3 \cdot 10^{-3}$	$\mathrm{W\,(^\circ C)^{-1}}$
α_3	$15 \cdot 10^{-3}$	$\mathrm{W\,(^\circ C)^{-1}}$
α_4	$125 \cdot 10^{-3}$	W
β_1	250	$\mathrm{W\,K^{-1}}$
β_2	7.8	$\mathrm{W\,K^{-1}}$
γ_1	50	$\mathrm{W\,(^\circ C)^{-1}}$
γ_2	400	W
γ_3	20	$\mathrm{W\,(^\circ C)^{-1}}$
κ_1	80	W
κ_2	0.4	$\mathrm{W\,rpm^{-1}}$
κ_3	16	$\mathrm{W\,(^\circ C)^{-1}}$
κ_4	1	$\mathrm{W\,(^\circ C)^{-1}}$
κ_5	120	W
κ_6	360	W
χ_1	$40 \cdot 10^{-3}$	$\mathrm{K\,W^{-1}}$
χ_2	35	$\mathrm{s^{-1}}$
χ_3	$230 \cdot 10^{-6}$	$\mathrm{K\,(W\,s)^{-1}}$
ξ_1	$175 \cdot 10^{-6}$	$\mathrm{K\,(W\,s)^{-1}}$
ξ_2	$45 \cdot 10^{-3}$	$\mathrm{s^{-1}}$
ξ_3	$25 \cdot 10^{-3}$	$\mathrm{s^{-1}}$
ξ_4	$25 \cdot 10^{-3}$	$\mathrm{s^{-1}}$
ζ_1	$6.25 \cdot 10^{-3}$	$\mathrm{s^{-1}}$

K = Kelvin; C = Celsius, W = Watt, s = second, rpm = revolutions per minute.

ACKNOWLEDGMENT

The authors would like to thank PRODUCTBLOKS GmbH in Korneuburg, Austria. The authors acknowledge TU Wien Bibliothek for financial support through its Open Access Funding Programme.

REFERENCES

[1] O. Adekomaya, T. Jamiru, R. Sadiku, and Z. Huan, "Sustaining the shelf life of fresh food in cold chain—A burden on the environment," *Alexandria Eng. J.*, vol. 55, no. 2, pp. 1359–1365, Jun. 2016.

[2] F. Bagheri, M. A. Fayazbakhsh, and M. Bahrami, "Real-time performance evaluation and potential GHG reduction in refrigerated trailers," *Int. J. Refrig.*, vol. 73, pp. 24–38, Jan. 2017. [Online]. Available: https://www.sciencedirect.com/science/article/pii/S0140700716302882

[3] H. M. Stellingwerf, A. Kanellopoulos, J. G. A. J. van der Vorst, and J. M. Bloemhof, "Reducing CO_2 emissions in temperature-controlled road transportation using the LDVRP model," *Transp. Res. D, Transp. Environ.*, vol. 58, pp. 80–93, Jan. 2018. [Online]. Available: https://www.sciencedirect.com/science/article/pii/S1361920917303735

[4] S. J. James, C. James, and J. A. Evans, "Modelling of food transportation systems—A review," *Int. J. Refrig.*, vol. 29, no. 6, pp. 947–957, Sep. 2006.

[5] S. Estrada-Flores and A. Eddy, "Thermal performance indicators for refrigerated road vehicles," *Int. J. Refrig.*, vol. 29, no. 6, pp. 889–898, Sep. 2006. [Online]. Available: https://www.sciencedirect.com/science/article/pii/S0140700706000958

[6] P. Neittaanmäki, K. Akimov, V. Akimova, and R. Tuovinen, "Challenges and current solutions of refrigerated transportation," in *Advanced Computational Methods and Design for Greener Aviation*. Springer, 2024, pp. 241–256.

[7] H. Assellaou, O. Souissi, M. Assellaou, and F. Mougli, "A logistic 4.0: A review of optimal temperature control problems in refrigerated transport systems," in *Proc. 1st Int. Conf. Cyber Manage. Eng. (CyMaEn)*, May 2021, pp. 1–6.

[8] S. Hou, H. Yin, F. Xu, P. Benjamín, J. Gao, and H. Chen, "Multihorizon predictive energy optimization and lifetime management for connected fuel cell electric vehicles," *Energy*, vol. 266, Mar. 2023, Art. no. 126466.

[9] Q. Hu, M. R. Amini, I. Kolmanovsky, J. Sun, A. Wiese, and J. B. Seeds, "Multihorizon model predictive control: An application to integrated power and thermal management of connected hybrid electric vehicles," *IEEE Trans. Control Syst. Technol.*, vol. 30, no. 3, pp. 1052–1064, May 2022.

[10] M. R. Amini, H. Wang, X. Gong, D. Liao-McPherson, I. Kolmanovsky, and J. Sun, "Cabin and battery thermal management of connected and automated HEVs for improved energy efficiency using hierarchical model predictive control," *IEEE Trans. Control Syst. Technol.*, vol. 28, no. 5, pp. 1711–1726, Sep. 2019.

[11] E. Luchini, A. Schirrer, and M. Kozek, "A hierarchical MPC for multi-objective mixed-integer optimisation applied to redundant refrigeration circuits," *IFAC-PapersOnLine*, vol. 50, no. 1, pp. 9058–9064, Jul. 2017.

[12] M. Fallmann, M. Lösch, A. Poks, and M. Kozek, "Energy-efficient hybrid model predictive control of mobile refrigeration systems," *Appl. Thermal Eng.*, vol. 235, Nov. 2023, Art. no. 121347. [Online]. Available: https://www.sciencedirect.com/science/article/pii/S1359431123013765

[13] D. Ramsey, A. Bouscayrol, L. Boulon, A. Desreveaux, and A. Vaudrey, "Flexible simulation of an electric vehicle to estimate the impact of thermal comfort on the energy consumption," *IEEE Trans. Transp. Electrific.*, vol. 8, no. 2, pp. 2288–2298, Jun. 2022.

[14] F. Fabris, P. Artuso, S. Marinetti, S. Minetto, and A. Rossetti, "Cooling unit impact on energy and emissions of a refrigerated light truck," *Appl. Thermal Eng.*, vol. 216, Nov. 2022, Art. no. 119132. [Online]. Available: https://www.sciencedirect.com/science/article/pii/S1359431122010638

[15] A. Poks, E. Luchini, F. Kitanoski, and M. Kozek, "Wholistic simulation of an all-electric refrigerated delivery vehicle," in *Proc. SICE Int. Symp. Control Syst. (SICE ISCS)*, Mar. 2020, pp. 1–6. [Online]. Available: https://ieeexplore.ieee.org/document/9083498

[16] M. Dellermann, O. Gehring, and O. Zirn, "Optimal control of energy flow between electrified auxiliaries and powertrain in hybrid-electric heavy-duty vehicles," in *Proc. Amer. Control Conf. (ACC)*, Jul. 2020, pp. 4161–4168.

[17] M. R. Amini, I. Kolmanovsky, and J. Sun, "Hierarchical MPC for robust eco-cooling of connected and automated vehicles and its application to electric vehicle battery thermal management," *IEEE Trans. Control Syst. Technol.*, vol. 29, no. 1, pp. 316–328, Jan. 2021.

[18] M. Liebers, R. Kloß, and B. Bäker, "Combined power train and thermal management optimization using an extended dynamic programming," in *16. Internationales Stuttgarter Symposium: Automobil-Und Motorentechnik*, Cham, Switzerland: Springer, 2016, pp. 367–381.

[19] H. Wang, M. R. Amini, Q. Hu, I. Kolmanovsky, and J. Sun, "Eco-cooling control strategy for automotive air-conditioning system: Design and experimental validation," *IEEE Trans. Control Syst. Technol.*, vol. 29, no. 6, pp. 2339–2350, Nov. 2021.

[20] M. R. Amini, J. Sun, and I. Kolmanovsky, "Two-layer model predictive battery thermal and energy management optimization for connected and automated electric vehicles," in *Proc. IEEE Conf. Decis. Control (CDC)*, Dec. 2018, pp. 6976–6981.

[21] M. Fallmann, A. Poks, and M. Kozek, "Hybrid model-based online estimation of air temperature in mobile small-scale cooling chambers," *Appl. Thermal Eng.*, vol. 208, May 2022, Art. no. 118147, doi: 10.1016/j.applthermaleng.2022.118147.

[22] A. Poks, M. Fallmann, L. Fink, L. Rinnofner, and M. Kozek, "Fault detection and isolation for a secondary loop refrigeration system," *Appl. Thermal Eng.*, vol. 227, Jun. 2023, Art. no. 120277, doi: 10.1016/j.applthermaleng.2023.120277.

[23] M. Lösch, M. Fallmann, A. Poks, and M. Kozek, "Simulation-based sizing of a secondary loop cooling system for a refrigerated vehicle," *Energies*, vol. 16, no. 18, p. 6459, Sep. 2023. [Online]. Available: https://www.mdpi.com/1996-1073/16/18/6459

[24] Y. Wang, Z. Sun, X. Li, X. Yang, and Z. Chen, "A comparative study of power allocation strategies used in fuel cell and ultracapacitor hybrid systems," *Energy*, vol. 189, Dec. 2019, Art. no. 116142. [Online]. Available: https://www.sciencedirect.com/science/article/pii/S0360544219318377

[25] Q. Hu, M. R. Amini, H. Wang, I. Kolmanovsky, and J. Sun, "Integrated power and thermal management of connected HEVs via multi-horizon MPC," in *Proc. Amer. Control Conf. (ACC)*, Jul. 2020, pp. 3053–3058.

[26] Q. Hu, M. R. Amini, A. Wiese, J. B. Seeds, I. Kolmanovsky, and J. Sun, "A multirange vehicle speed prediction with application to model predictive control-based integrated power and thermal management of connected hybrid electric vehicles," *J. Dyn. Syst., Meas., Control*, vol. 144, no. 1, Jan. 2022, Art. no. 011105.

[27] E. Luchini, A. Poks, D. Radler, and M. Kozek, "Model predictive temperature control for a food transporter with door-openings," in *Proc. SICE Int. Symp. Control Syst. (SICE ISCS)*, Mar. 2020, pp. 85–91. [Online]. Available: https://ieeexplore.ieee.org/document/9083491

[28] C. Du, S. Huang, Y. Jiang, D. Wu, and Y. Li, "Optimization of energy management strategy for fuel cell hybrid electric vehicles based on dynamic programming," *Energies*, vol. 15, no. 12, p. 4325, Jun. 2022. [Online]. Available: https://www.mdpi.com/1996-1073/15/12/4325

[29] Y. Liu, J. Liang, J. Song, and J. Ye, "Research on energy management strategy of fuel cell vehicle based on multi-dimensional dynamic programming," *Energies*, vol. 15, no. 14, p. 5190, Jul. 2022. [Online]. Available: https://www.mdpi.com/1996-1073/15/14/5190

[30] A. Ferrara, S. Jakubek, and C. Hametner, "Energy management of heavy-duty fuel cell vehicles in real-world driving scenarios: Robust design of strategies to maximize the hydrogen economy and system lifetime," *Energy Convers. Manage.*, vol. 232, Mar. 2021, Art. no. 113795.

[31] K. D. Nguyen, S. Sermeno, M. T. Pham, P. Le, and E. B. Brusq, "Impact analysis of the electrified auxiliary system on HEV/PHEV energy efficiency," in *Proc. ICEEV*, Dresden, Germany, Jun. 2015. [Online]. Available: https://hal.science/hal-02163478

[32] R. Abdrakhmanov and L. Adouane, "Efficient ACC with stop&go maneuvers for hybrid vehicle with online sub-optimal energy management," in *Proc. 11th Int. Workshop Robot Motion Control (RoMoCo)*, Jul. 2017, pp. 7–14.

[33] S. Bao, P. Sun, J. Zhu, Q. Ji, and J. Liu, "Improved multi-dimensional dynamic programming energy management strategy for a vehicle power-split hybrid powertrain," *Energy*, vol. 256, Oct. 2022, Art. no. 124682.

[34] A. M. Ali, A. Ghanbar, and D. Söffker, "Optimal control of multi-source electric vehicles in real time using advisory dynamic programming," *IEEE Trans. Veh. Technol.*, vol. 68, no. 11, pp. 10394–10405, Nov. 2019.

[35] M. R. Mes and A. P. Rivera, "Approximate dynamic programming by practical examples," in *Markov Decision Processes in Practice*. Cham, Switzerland: Springer, 2017.

[36] A. Chehri, N. Quadar, and R. Saadane, "Communication and localization techniques in vanet network for intelligent traffic system in smart cities: A review," in *Proc. 3rd KES-STS Int. Symp. Smart Transp. Syst.*, Cham, Switzerland: Springer, 2020, pp. 167–177.
[37] M. N. Tahir, P. Leviäkangas, and M. Katz, "Connected vehicles: V2V and V2I road weather and traffic communication using cellular technologies," *Sensors*, vol. 22, no. 3, p. 1142, Feb. 2022. [Online]. Available: https://www.mdpi.com/1424-8220/22/3/1142
[38] L. Zhou and M. Preindl, "Bidirectional transformerless EV charging system via reconfiguration of 4×4 drivetrain," in *Proc. IEEE Energy Convers. Congr. Expo. (ECCE)*, Sep. 2018, pp. 3923–3927.
[39] S. Habib, M. M. Khan, F. Abbas, and H. Tang, "Assessment of electric vehicles concerning impacts, charging infrastructure with unidirectional and bidirectional chargers, and power flow comparisons," *Int. J. Energy Res.*, vol. 42, no. 11, pp. 3416–3441, Sep. 2018.
[40] M. Mitschke and H. Wallentowitz, *Dynamik Der Kraftfahrzeuge*, vol. 4. Cham, Switzerland: Springer, 1972.
[41] I. Preda, D. Covaciu, and G. Ciolan, "Coast down test—Theoretical and experimental approach," Transilvania Univ. Press, Oct. 2010, doi: 10.13140/RG.2.1.4048.5925. [Online]. Available: https://api.semanticscholar.org/CorpusID:24855595
[42] L. Guzzella and A. Sciarretta, *Vehicle Propulsion Systems*, vol. 1. Cham, Switzerland: Springer, 2007.
[43] K. Liu, K. Li, Q. Peng, and C. Zhang, "A brief review on key technologies in the battery management system of electric vehicles," *Frontiers Mech. Eng.*, vol. 14, no. 1, pp. 47–64, Mar. 2019.
[44] D. Thiruvonasundari and K. Deepa, "Electric vehicle battery modelling methods based on state of charge–review," *J. green Eng.*, vol. 10, no. 1, pp. 24–61, 2020.
[45] E. Mizutani and S. Dreyfus, "A tutorial on the art of dynamic programming for some issues concerning Bellman's principle of optimality," *ICT Exp.*, vol. 9, no. 6, pp. 1144–1161, Dec. 2023.
[46] D. Bertsekas, *Abstract Dynamic Programming*. Belmont, MA, USA: Athena Scientific, 2022.
[47] N. Murgovski, L. Johannesson, J. Sjöberg, and B. Egardt, "Component sizing of a plug-in hybrid electric powertrain via convex optimization," *Mechatronics*, vol. 22, no. 1, pp. 106–120, Feb. 2012.
[48] M. Ansarey, M. Shariat Panahi, H. Ziarati, and M. Mahjoob, "Optimal energy management in a dual-storage fuel-cell hybrid vehicle using multi-dimensional dynamic programming," *J. Power Sources*, vol. 250, pp. 359–371, Mar. 2014. [Online]. Available: https://www.sciencedirect.com/science/article/pii/S0378775313018284
[49] S. Kofler, Z. P. Du, S. Jakubek, and C. Hametner, "Adaptive step size dynamic programming for optimal energy management of fuel cell vehicles," in *Proc. IEEE Vehicle Power Propuls. Conf. (VPPC)*, Oct. 2023, pp. 1–6.
[50] F. Borrelli, A. Bemporad, and M. Morari, *Predictive Control for Linear and Hybrid Systems*. Cambridge, U.K.: Cambridge Univ. Press, 2017.
[51] A. Zhakatayev, B. Rakhim, O. Adiyatov, A. Baimyshev, and H. A. Varol, "Successive linearization based model predictive control of variable stiffness actuated robots," in *Proc. IEEE Int. Conf. Adv. Intell. Mechtron. (AIM)*, Jul. 2017, pp. 1774–1779.
[52] M. H. Murillo, A. C. Limache, P. S. Rojas Fredini, and L. L. Giovanini, "Generalized nonlinear optimal predictive control using iterative state-space trajectories: Applications to autonomous flight of UAVs," *Int. J. Control, Autom. Syst.*, vol. 13, no. 2, pp. 361–370, Apr. 2015.
[53] Gurobi Optimization, LLC. (2023). *Gurobi Optimizer Reference Manual*. [Online]. Available: https://www.gurobi.com
[54] J. A. E. Andersson, J. Gillis, G. Horn, J. B. Rawlings, and M. Diehl, "CasADi: A software framework for nonlinear optimization and optimal control," *Math. Program. Comput.*, vol. 11, no. 1, pp. 1–36, Mar. 2019.
[55] C. Caldwell, E. Collins, and S. Palanki, "Integrated guidance and control of AUVs using shrinking horizon model predictive control," in *Proc. OCEANS*, Sep. 2006, pp. 1–6.
[56] *Nissan E-nv200 Van Brochure*. Accessed: Sep. 9, 2024. [Online]. Available: https://www-europe.nissan-cdn.net/content/dam/Nissan/gb/brochures/Vehicles/Nissan_e-NV200_van_UK.pdf
[57] X. Wei, M. Yimin, and Z. Feng, "Identification of parameters in li-ion battery model by least squares method with variable forgetting factor," *Int. J. Comput. Methods*, vol. 17, no. 7, Sep. 2020, Art. no. 1950027.
[58] A. Braun and W. Rid, "The influence of driving patterns on energy consumption in electric car driving and the role of regenerative braking," *Transp. Res. Proc.*, vol. 22, pp. 174–182, Jan. 2017. [Online]. Available: https://www.sciencedirect.com/science/article/pii/S235214651730159X
[59] Solcast. (2024). *Global Solar Irradiance Data and Pv System Power Output Data*. [Online]. Available: https://solcast.com/
[60] E. Luchini and M. Kozek, "Disturbance observer and ageing estimation for a temperature controlled food transporter," in *Proc. SICE Int. Symp. Control Syst. (SICE ISCS)*, Mar. 2018, pp. 97–104.
[61] M. Killian and M. Kozek, "Short-term occupancy prediction and occupancy based constraints for MPC of smart homes," *IFAC-PapersOnLine*, vol. 52, no. 4, pp. 377–382, 2019.
[62] H. Fu, S. Huang, Y. Li, J. Cheng, Y. Guo, K. Wang, and R. Sun, "The research and application of technology and core components in commercial refrigeration and freezing Systems: A review," *J. Stored Products Res.*, vol. 108, Sep. 2024, Art. no. 102400.
[63] X. Wu, S. Hu, and S. Mo, "Carbon footprint model for evaluating the global warming impact of food transport refrigeration systems," *J. Cleaner Prod.*, vol. 54, pp. 115–124, Sep. 2013.
[64] F. Fabris, M. Fabrizio, S. Marinetti, A. Rossetti, and S. Minetto, "Evaluation of the carbon footprint of HFC and natural refrigerant transport refrigeration units from a life-cycle perspective," *Int. J. Refrig.*, vol. 159, pp. 17–27, Mar. 2024.

AGNES POKS (Member, IEEE) received the M.S. degree in electrical engineering, in 2019, and the Ph.D. degree, in 2020. In her Diploma thesis, she worked on sensorless estimation and control for a permanent synchronous machine. In her Ph.D. thesis, she develops advanced modeling, control, and observation concepts for thermal energy systems for electric vehicles. Since 2019, she has been a Research Assistant with the Research Unit for Control Engineering and Process Automation, Institute of Mechanics and Mechatronics, Vienna University of Technology (TU Wien).

ALEXANDER SCHIRRER received the M.S. degree in mechanical engineering and the Ph.D. and Habilitation degrees from Vienna University of Technology (TU Wien), Vienna, Austria, in 2007, 2011, and 2018, respectively. As a Postdoctoral Researcher and a Teacher, since 2011, and in the role of a Senior Scientist with the Institute of Mechanics and Mechatronics, TU Wien, since 2023, he teaches various graduate-level control and engineering lectures and drives basic and applied research in modeling, simulation, optimization, and control of complex and distributed-parameter systems.

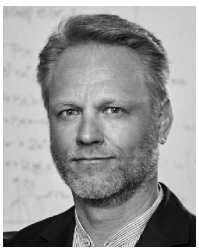

MARTIN KOZEK received the M.S. degree in mechanical engineering, the Ph.D. degree, and the Habilitation degree from Vienna University of Technology, Vienna, Austria, in 1994, 2000, and 2009, respectively. He is currently a Professor with the Institute of Mechanics and Mechatronics, Vienna University of Technology. His research interests include nonlinear systems modeling and identification, model-predictive process control, and active control of structural vibrations.